6-1-2011

Modeling the capacitive behavior of coplanar striplines and coplanar waveguides using simple functions

Jeffrey Abbott

MODELING THE CAPACITIVE BEHAVIOR OF COPLANAR STRIPLINES AND COPLANAR WAVEGUIDES USING SIMPLE FUNCTIONS

by

JEFFREY TOWNSLEY ABBOTT

A Thesis Submitted in Partial Fulfillment of the
Requirements for the Degree of
Master of Science
in
Electrical Engineering
at the
Rochester Institute of Technology

Approved by:

_____
Advisor: Dr. Robert J. Bowman

_____
Member: Dr. James E. Moon

_____
Member: Dr. Karl D. Hirschman

_____
Department Head: Dr. Sohail A. Dianat

Department of Electrical and Microelectronic Engineering
Kate Gleason College of Engineering
Rochester Institute of Technology
Rochester, New York
June 2011

Thesis Release Permission

DEPARTMENT OF ELECTRICAL AND MICROELECTRONIC ENGINEERING

COLLEGE OF ENGINEERING

ROCHESTER INSTITUTE OF TECHNOLOGY

ROCHESTER NY

JUNE, 2011

Title of Thesis:

MODELING THE CAPACITIVE BEHAVIOR OF COPLANAR STRIPLINES AND COPLANAR WAVEGUIDES USING SIMPLE FUNCTIONS

I, Jeffrey Townsley Abbott, hereby grant permission to Wallace Memorial Library of the Rochester Institute of Technology to reproduce this thesis in whole or in part. Any reproduction will not be for commercial use or profit.

Signature of Author: _____ Date: _____

ABSTRACT
Kate Gleason College of Engineering
Rochester Institute of Technology

Degree: Master of Science

Program: Electrical Engineering

Author: Jeffrey Townsley Abbott

Title: Modeling the Capacitive Behavior of Coplanar Striplines and Coplanar Waveguides Using Simple Functions

The coplanar waveguide (CPW) structure has been popular for Monolithic Microwave Integrated Circuit (MMIC) design due to the wide versatility of its designable impedance. Since its introduction in 1969, it has been utilized in a wide range of applications and consequently has been analyzed extensively for its electrical characteristics. Other planar structures with similar geometries have also received much attention, including the conductor-backed coplanar waveguide (CBCPW) and coplanar stripline (CPS). A common approach for analyzing these planar structures, assuming quasi-TEM mode of operation, involves the use of conformal mapping techniques. The traditional conformal mappings realize special functions allowing for problems of convergence, computation efficiency, and accuracy during implementation in CAD software.

The focus of this thesis is modeling the capacitive behavior of planar devices including the conductor-backed interdigital coplanar waveguide (CBICPW), CPS, and finite-width conductor-backed coplanar waveguide (FWCBCPW) in an infinite well under a quasi-TEM mode of operation. Continuously differentiable, simple functions are used in place of special functions to improve the performance of models within CAD environments. New conformal mapping techniques are introduced that use only simple functions. Combined with other approximations, one can formulate expressions with arbitrary accuracy. A new iterative expression is presented for evaluation of the elliptic integrals ratio, *K/K'*, commonly used in standard expressions for planar structures. The new expression, based on a continuously differentiable function, exhibits a relative error on the order of 10^{-11} with reduced computational complexity. Results from the new models are compared to the simulated results of a commercial electromagnetic field solver. Experimental results that were available for the CBICPW structure indicated good correspondence to results calculated from the new model.

Acknowledgements

There are many people that I would like to acknowledge for helping in the completion of this thesis and my graduate/undergraduate education.

I would like to thank my advisor Dr. Robert Bowman for his guidance, patience, and overwhelming drive to explore new ideas. Under his supervision, I was able to dive into topic areas unbeknownst to me prior to doing research in the ADIML laboratory. Not only has he taught me a vast number of technical skills and abilities, he has also showed me how to express my thoughts more clearly, "What exactly are you trying to say?" is constantly running through my head. My ideas just come out backwards, when I'm writing that is. I will always appreciate his support and wisdom in all areas of my education.

Many thanks go to Dr. Moon and Dr. Hirschman for participating on my committee and reviewing this thesis. I would also like to thank Dr. Moon for the numerous numbers of classes that he has taught me, comprising most of my exposure to device physics, MEMs, and basic electronics. I can only hope to one day be as good of a teacher, critical thinker, and mentor as Dr. Moon.

It is a pleasure to thank Dr. Joseph Revelli and Dr. Christopher Nassar for their answers to my unending number of questions regarding mathematics and applied physics. My excitement for new ideas and questions without easy answers is sometimes overwhelming, but both of their patience and rational have taught me to examine complex topics in a new light.

I owe my deepest gratitude to my mother and father for their unending support throughout my education. Their rational thinking, emotional outlooks, and utter compassion have inspired me to be more than I ever could have expected. I will be eternally grateful for all the opportunities they have provided for me.

This thesis would not have been possible without the love and support from AnnMarie throughout my graduate experience at RIT. Her phone calls late at night often saved me from starvation and reminded me that sleep is just as important as elliptic integrals. The numerous weekends spent at the lab together made the process exponentially more enjoyable. I truly appreciate all that she has done for me.

Lastly, I would like to show my gratitude to Michael O'Dell, Dan Pulito, Christopher Everson, Joshua Winterkorn, and Virag Chaware for their support and friendship throughout my studies. I would also like to thank and acknowledge the support from the rest of my family: Michael, Rosalyn, and Katie Abbott, with Peter Beauregard of course.

In memory of my father, James Cameron Abbott

Contents

List of Figures

Nomenclature

CBCPW	Conductor-backed coplanar waveguide
CBICPW	Conductor-backed interdigital coplanar waveguide
CPS	Coplanar stripline
CPW	Coplanar waveguide
CMU	Capacitance measurement unit
FWCBCPW	Finite-width conductor-backed coplanar waveguide
ICPW	Interdigital coplanar waveguide
IDC	Interdigital capacitor
K/K'	Elliptic integrals ratio

List of Symbols

ε_0	Permittivity of free space
ε_r	Relative permittivity of interface dielectric
$\varsigma(k)$	Estimation of the elliptic integrals ratio
φ	Potential field for Laplace's equation
A	Intermediate variable in CPS conformal mapping
a	Intermediate variable in FWCBCPW conformal mapping
B	Intermediate variable in CPS conformal mapping
b	Intermediate variable in FWCBCPW conformal mapping

C Capacitance

C_3 Simplification of C_{13} and C_{23} due to symmetry

C^a Capacitance with dielectrics replaced by air

C_{ID} Interdigital capacitance

C_{i0} Parasitic capacitance between conduction plane i and ground

C_{ij} Hybrid-pi capacitance between conduction planes i and j

C_{meas} Measured capacitance from CMU

C' Capacitance per unit length

C'_{air} Capacitance per unit length of air for FWCBCPW

C'_{ID} Interdigital capacitance per unit length

C'_{below} Capacitance per unit length of dielectric region of FWCBCPW

C'_{ID_∞} Interdigital capacitance per unit length of a CBCPW with infinite-width conductors

C'_{ij} Hybrid-pi capacitance per unit length between conduction planes i and j

C'_{well} Capacitance per unit length of CPS in an infinite well

C'_{∞} Capacitance per unit length of a CBCPW with infinite-width conduction planes

c Speed of light

c_0 Intermediate variable in FWCBCPW conformal mapping

D Intermediate variable in CPS conformal mapping

D_1 Intermediate variable in CPS conformal mapping

d Intermediate variable in FWCBCPW conformal mapping

$F(\varphi|k)$ Incomplete elliptic integral of the first kind evaluated using the elliptic modulus

$f(q)$ Function used in iterative solution

g Conductor gap

h Interface dielectric thickness

$K(k)$ Complete elliptic integral of the first kind evaluated using the modulus k

k Elliptic modulus

$K'(k)$ Complement of the complete elliptic integral of the first kind, $K(k')=K'(k)$

k' Complement of the elliptic modulus where $k' = \sqrt{1-k^2}$

l Length of interdigital fingers

l_{eff} Effective length of CBICPW structure

m Intermediate variable in FWCBCPW conformal mapping

N Number of interdigital fingers

n Number of iterations

q Intermediate variable in CPS conformal mapping

w Conductor width

Q_i Charge on conduction plane i

V_i Potential on conduction plane i

V_o Potential applied to establish effective capacitance

V_s Applied voltage from CMU

V_x Unknown potential on substrate conduction plane

v_{ph} Phase velocity

Z_0 Characteristic impedance

Z_{meas} Measured impedance from CMU

Chapter 1

Introduction

Transmission lines are an integral component for designing high-frequency circuits for both wired and wireless applications. Four major classifications of transmission lines have become popular for designing Monolithic Microwave Integrated Circuits (MMICs) including the microstrip, slotline, coplanar waveguide (CPW), and coplanar stripline (CPS) [1]. Comparisons have been made between the four types of transmission lines with each type having their own benefits and drawbacks [1][2][3]. A summary of the reported designable range for the characteristic impedance, Z_0, and ease of implementation can be seen in Table 1.

The wide versatility in its designable impedance has made the CPW ideal for many microwave circuit designers. Since its introduction in 1969 [4], the structure has been used for a

	Lower Limit for Z_0 (Ω) at 30 GHz	**Upper Limit for Z_0 (Ω) at 30 GHz**	**Parallel Component Integration**	**Series Component Integration**
Microstrip	11	110	Poor	Easy
Slotline	35	250	Easy	Difficult
CPW	20	250	Easy	Easy
CPS	20	250	Easy	Easy

Table 1. Comparison of properties of various transmission lines.

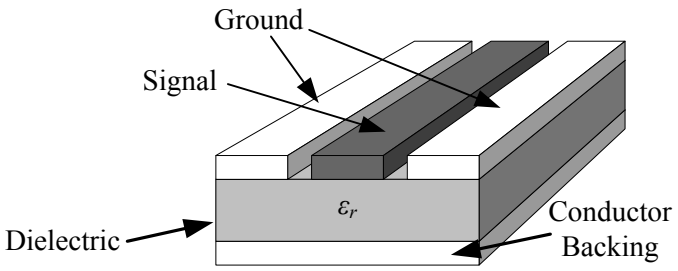

Fig. 1.1. A basic coplanar waveguide structure with conductor backing.

wide number of applications [5][6][7][8][9][10][11]. Other planar structures with similar geometries have received much attention as well, including the conductor-backed coplanar waveguide (CBCPW) and the interdigital capacitor (IDC). A new device, the conductor-backed interdigital coplanar waveguide (CBICPW), has also been under investigation for uses with thin-film silicon process technologies on glass [12] and will be discussed in this thesis.

A basic representation of a CBCPW is illustrated in Fig. 1.1. For most applications, a signal metal line is routed between two ground metal lines on top of a dielectric material. A conductor backing below the dielectric material is optional but offers the improvement of mechanical strength and heat dissipation while enabling easy implementation of mixed coplanar/microstrip circuits [13]. A dielectric thickness twice to three times the width of the slots is recommended in conjunction with a high dielectric permittivity to permit proper propagation of the wave without being disturbed by an interface on the backside [4].

Simple analyses for the electrical parameters of planar structures assume a quasi-TEM mode where the propagating wavelength is much larger than the device dimensions, resulting in electric and magnetic fields transverse to the direction of the wave. More rigorous methods use full-wave analysis techniques which allow for frequency dependence of phase velocity and characteristic impedance. Under both of these conditions, the electrical parameters of the CPW,

CBCPW, CPS, and IDC have been well characterized in the literature. Various techniques include conformal mapping [12][14][15][16][17][18][19][20][21][22][23][24], 3D Finite Difference Time Domain (FDTD) Method [25][26][27][28], Spectral Domain Method [13][29][30], Integral Method [31][32], Transverse Resonance Technique [33], Relaxation Method [34], and Multilayer Perceptron Neural Networks (MLPNNs) [35]. Many of these methods result in accurate calculations of the desired electrical parameters with varying degrees of complexity, computation time, and ease of implementation.

The bulk of the work in this thesis rests in modeling the capacitive behavior of planar devices including the CBICPW, CPS, and finite-width conductor-backed coplanar waveguide (FWCBCPW) in an infinite well under a quasi-TEM mode of operation. Under this approximation, the relative permittivity, ε_r, phase velocity, v_{ph}, and characteristic impedance can be expressed as [1],

$$\varepsilon_r = \frac{C}{C^a} \tag{1.1}$$

$$v_{ph} = \frac{c}{\sqrt{\varepsilon_r}} \tag{1.2}$$

$$Z_0 = \frac{1}{C v_{ph}} = \frac{1}{c\sqrt{\varepsilon_r} C^a} \tag{1.3}$$

where c is the speed of light, C is the total capacitance, and C^a is the capacitance of the corresponding line with all the dielectrics replaced by air. Therefore, with solutions for capacitance, the corresponding characteristic impedance and relative permittivity can be calculated.

1.1 The Need for a CBICPW and FWCBCPW Capacitance Model

Thompson et al. has analyzed the quasi-TEM parameters of the non-conductor-backed interdigital coplanar waveguide (ICPW) using finite-element analysis [28]. The benefits reported by the authors for the ICPW include lower characteristic impedance for the same minimum feature size and overall line width, reduced high-frequency resistive loss, and greater reduction in ohmic losses for thickening the conductors as compared to the traditional CPW. These benefits, combined with those previously mentioned for conductor backing, offer promise for the CBICPW and provide motivation for characterizing its behavior.

Previous work in modeling interdigital devices for their capacitance has been in the field of IDCs. A simple top-down view of a set of interdigital fingers is shown in Fig. 1.2(a). The most common approach assumes a uniform cross-sectional field for the length of the fingers, resulting in the cross-sectional view in Fig. 1.2(b). This assumption allows for the use of two dimensional equations to calculate the capacitance per unit length of the cross section and then multiply it by the length of the finger to calculate a capacitance. Additional capacitance contributions from the finger ends and outermost fingers are added to account for the non-uniform fields at the finger ends and on the outside edges of the device [19][23]. This technique offers accurate results with a wide range of physical device sizes and multiple substrates; the latter calculated using the

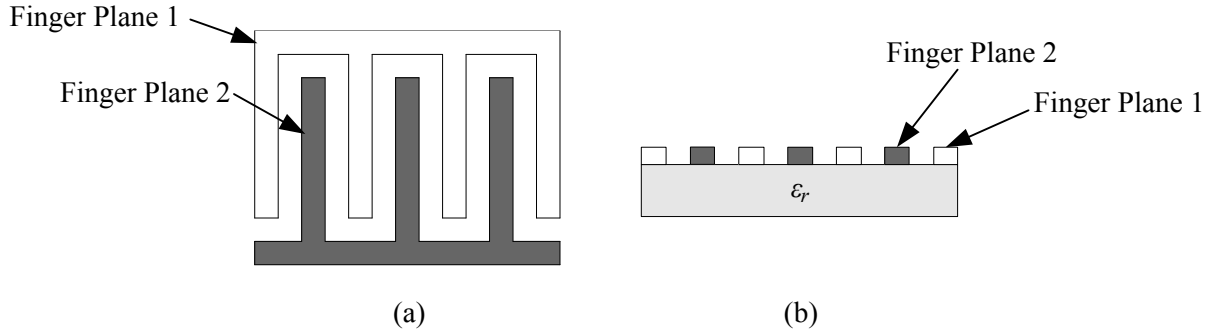

Fig. 1.2. Example of interdigital fingers showing (a) top-down view and (b) cross-sectional view along length of the fingers.

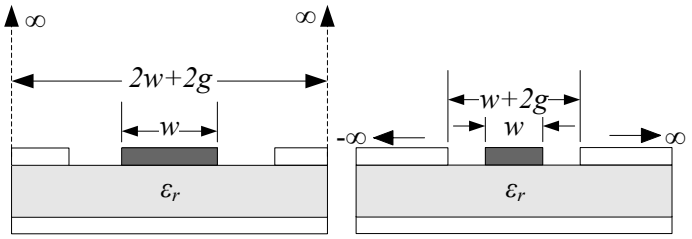

Fig. 1.3. Cross-sectional view of (a) FWCBCPW in an infinite well and (b) CBCPW with infinite lateral conduction planes.

partial capacitance technique [17][24]. The accurate results come at the cost of a fair amount of complexity added with determining the contributions of the finger ends and outermost fingers.

To use a similar approach for the CBICPW, the FWCBCPW in an infinite well can be used to calculate the cross-sectional capacitance per unit length. Two major limitations exist with this approach, however. The capacitance of the FWCBCPW in an infinite well, represented in Fig. 1.3(a), has not been modeled analytically due to its asymmetry, though the infinite-width CBCPW has been analyzed, Fig. 1.3(b), using conformal mapping techniques [12]. Assuming small gaps compared to the lateral conduction plane widths, the infinite-width equation can be used with minor error while limiting the devices dimensions that are applicable. An approximate capacitance model for the FWCBCPW in an infinite well will be introduced in this thesis but not used in conjunction with the CBICPW.

The second limitation arises with the ratio of hyperbolic tangents in the expression for the infinite-width CBCPW, displayed in (1.4), losing value at a lateral conductor width to dielectric thickness ratio of 24.3 for a standard PC using 64-bit double-precision floating-point variables.

$$
\begin{aligned}
C'_{\infty} &= 2\varepsilon_0 \left[\frac{K(k_0)}{K(k'_0)} + \varepsilon_r \frac{K(k_1)}{K(k'_1)} \right] \\
k_0 &= w/(w+2g) \\
k_1 &= \tanh(\pi w/4h)/\tanh(\pi(w+2g)/4h)
\end{aligned}
\tag{1.4}
$$

Consequently, for a thin-film device where this ratio can easily exceed 1000, this equation will lose value. As a result, to model the capacitance of the CBICPW, an expression for the capacitance of the FWCBCPW in an infinite well has to be established and must be capable of evaluation for all dielectric thicknesses. This thesis will approximate an expression for the capacitance of the CBICPW and provide a blending function for continuous evaluation with moderate accuracy.

1.2 The Need for Simple Function Evaluation

One of the most popular ways to develop analytical solutions for the electrical parameters of planar structures is to use conformal mapping techniques [12][14][15][16][17][18][19][20] [21][22][23][24]. These expressions, in the form of analytical solutions, are ideal for computer-aided design (CAD) orientated software. In addition, the dependency of the electrical parameters on various physical dimensions is clearly seen with a closed-form expression. Resulting expressions are easily differentiated, making them ideal for sensitivity analysis and predicting process variation. Many approximations show that these expressions can also be accurate up to frequencies of 20 GHz [17], comparable to full-wave techniques.

It is common to use Schwarz-Christoffel conformal mapping due to its ability to map the real axis of the complex plane onto the exterior of a simple polygon [36]. The upper half plane is correspondingly mapped to the interior of the polygon. This mapping is useful for solving the

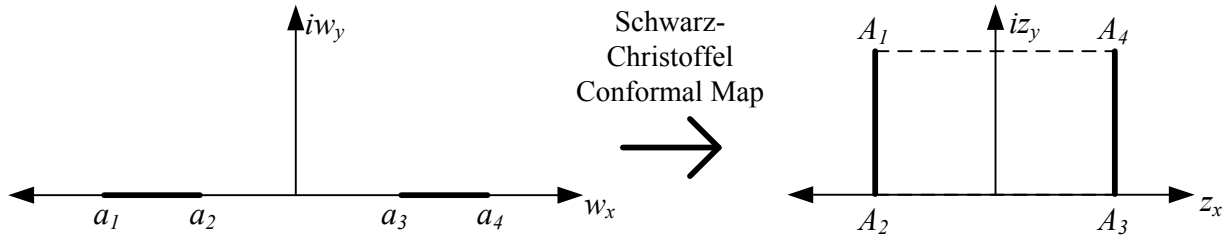

Fig. 1.4. Simple representation of a Schwarz-Christoffel transformation to a rectangular region.

electric and magnetic fields of complex geometries by mapping to simpler geometries such as infinite strips, parallel plate bounded geometries, and other known trivial solutions.

Mapping to a rectangular region, as depicted in Fig. 1.4, is ideal for two-conductor planar geometries to solve Laplace's equation for the electric field. The line-to-line capacitance, characteristic impedance, and relative permittivity can then be easily derived. Nonetheless, the device widths in this new simple region require the evaluation of the complete elliptic integral of the first kind, a special function, and its complement. For evaluation of parameters in CAD-orientated software, this special function often has to be specifically implemented allowing for potential problems with poor convergence and reduced computation efficiency and accuracy.

Hilberg published estimations in 1968 for the ratio of the complete elliptic integral of the first kind to its complement, *K/K'*, based on simple function conformal mappings [37]. The expressions use two regions of calculation with only simple functions resulting in a maximum relative accuracy of $3 \cdot 10^{-6}$. The precision of the expressions and simple implementation have made it a standard in calculating microstrip electrical parameters with references made in many popular text books [1][38].

The downside to these expressions is the need for two regions of calculation, resulting in a discontinuous derivative at the boundary with respective to the input physical dimensions. In addition, the steps followed to derive the expressions are not easily understood and offer little

help for further improvements. The evaluation of *K/K'* will be addressed in this thesis by using new simple function conformal mappings and other approximations. The new conformal mappings utilized are then applied to the FWCBCPW in an infinite well to demonstrate their flexibility.

1.3 Thesis Overview

The theory and simulations for capacitive modeling of the CBICPW are described in Chapter 2. Chapter 3 focuses on the experimental verification of the developed CBICPW model including the measurement technique. Chapter 4 describes the conformal mapping techniques used in place of a Schwarz-Christoffel Conformal Map and provides a computation comparison to other techniques available in the literature. Chapter 5 investigates similar conformal mapping techniques to those described in Chapter 4 to establish an approximate expression for the capacitance of the FWCBCPW in an infinite well. Finally, Chapter 6 provides an overall discussion of the work performed and offers suggestions for future work.

Chapter 2

Capacitive Modeling of CBICPW

As mentioned in Chapter 1, there is a need for a capacitive model for the interdigital capacitance of the conductor-backed interdigital coplanar waveguide (CBICPW). The initial strategy in this work was to empirically fit polynomial equations to simulated capacitance data from the finite difference field solver Ansoft MAXWELL™. The expressions derived from this effort provided accurate results to the range of physical dimensions simulated but provided incorrect calculations for dimensions outside the simulated range. The second approach, outlined in this chapter, seeks to use analytical expressions derived from first principles and previous research and extend it to the CBICPW.

2.1 General Overview and Definitions

Cross-sectional and top-down views of the CBICPW are shown in Fig. 2.1(a) and Fig. 2.1(b), respectively, with the physical device parameters shown. From Fig. 2.1, the height of the interface dielectric material is defined as h, the interface dielectric relative permittivity is ε_r, the width of the fingers is w, the spacing or gap between the fingers is g, the length of the

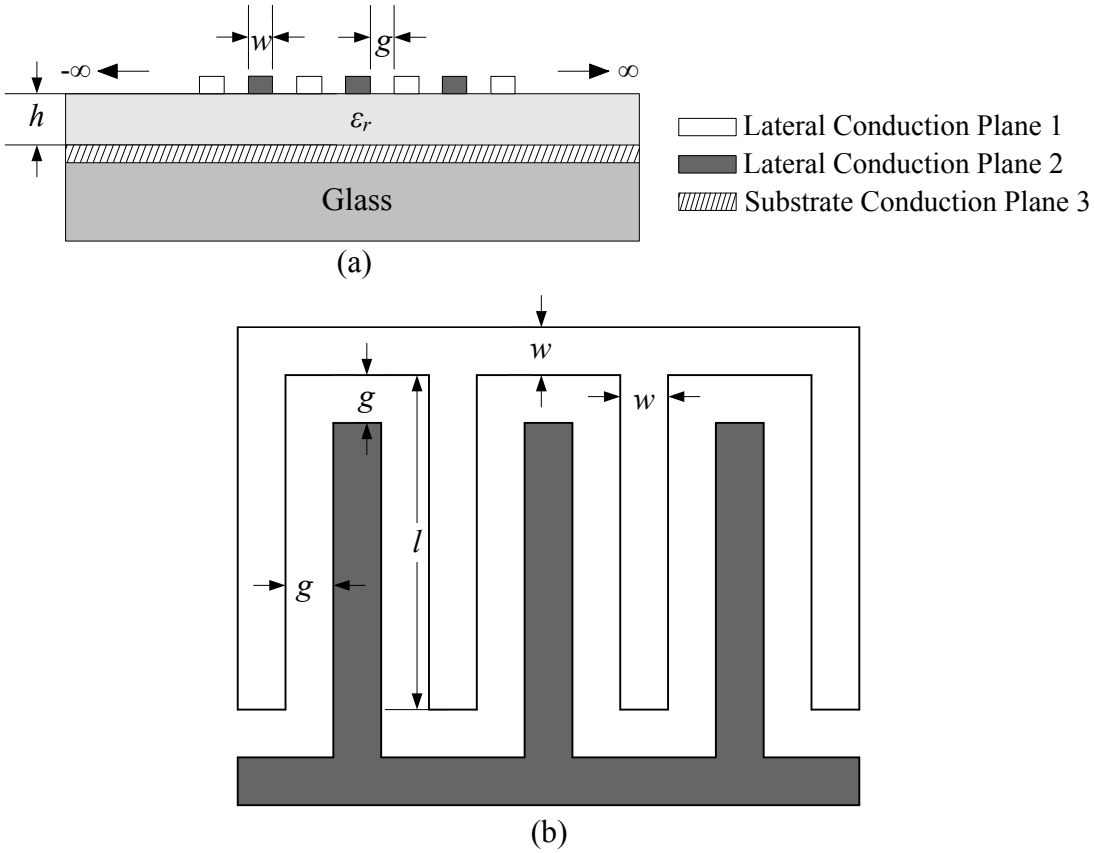

Fig. 2.1. (a) Cross-sectional view of CBICPW and (b) top-down view of CBICPW.

fingers is *l*, and the number of fingers is *N*. The CBICPW is placed upon a thick layer of glass (Fig. 2.1(a) is not drawn to scale), though no charge is assumed to be under the substrate conduction plane. The glass can therefore be ignored for the charge exchange of the system as there is no electric field in this region due to the infinite-width substrate conduction plane.

The charge exchange of the system can be modeled using a hybrid-pi capacitance model, represented in schematic form in Fig. 2.2. The charge on each plane can be calculated,

$$\begin{bmatrix} Q_1 \\ Q_2 \\ Q_3 \end{bmatrix} = \begin{bmatrix} C_{12}+C_3 & -C_{12} & -C_3 \\ -C_{12} & C_{12}+C_3 & -C_3 \\ -C_3 & -C_3 & 2C_3 \end{bmatrix} \begin{bmatrix} V_1 \\ V_2 \\ V_3 \end{bmatrix} \tag{2.1}$$

where

$C_3 = C_{13} = C_{23}$

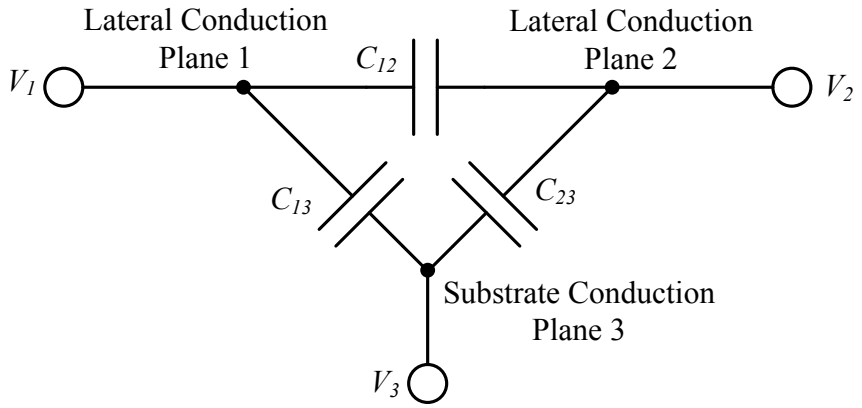

Fig. 2.2. Hybrid pi capacitance model for CBICPW.

where C_{ij} is the hybrid-pi capacitance between conduction plane i and plane j, Q_i is the charge on conduction plane i, and V_i is the potential of conduction plane i. The two finger planes are assumed to be symmetric (N is even) resulting in the capacitances C_{13} and C_{23} being equivalent and simplified to C_3. The interdigital capacitance between the two lateral conduction planes, C_{ID}, in terms of the hybrid-pi capacitance values can be expressed as C_{12} in parallel with the series combination of C_{13} and C_{23},

$$C_{ID} = C_{12} + \frac{C_{13}C_{23}}{C_{13} + C_{23}} = C_{12} + \frac{C_3}{2} \tag{2.2}$$

This definition of the interdigital capacitance assumes that the substrate conduction plane is floating with respect to the applied voltage across the lateral conduction planes with no net charge on the substrate conduction plane (Q_3=0). Under this assumption, the potential of the substrate conduction plane, V_3, can be derived by applying a voltage, V_o, across the lateral conduction planes,

$$V = \begin{bmatrix} V_o \\ 0 \\ V_3 \end{bmatrix} \tag{2.3}$$

The charge exchange can be calculated by using (2.1),

$$\begin{aligned} Q_1 &= (C_{12} + C_3)\cdot V_o - C_3 \cdot V_3 \\ Q_2 &= -C_{12} \cdot V_o - C_3 \cdot V_3 \\ Q_3 &= -C_3 \cdot V_o + 2C_3 \cdot V_3 \end{aligned} \tag{2.4}$$

Therefore, the potential V_3 may be solved for using Q_3=0 resulting in,

$$V_3 = \frac{V_o}{2} \tag{2.5}$$

To model the interdigital capacitance, a unit cell capacitance per unit length will be derived and multiplied by an effective length.

2.2 Unit Cell Development

The cross section of the CBICPW can be comprised of unit cells, due to the symmetry created by the repeated structure. Fig. 2.3(a) and Fig. 2.3(b) display the cross-sectional views of the CBICPW and FWCBCPW in an infinite well, respectively. A simulated potential field distribution for a cross section of a CBICPW is illustrated in Fig. 2.4. Magnetic walls can be placed along electric field lines to isolate regions, depicted in the plot by dashed lines. Therefore, placing multiple FWCBCPW in an infinite well in parallel, the cross section of the CBICPW is formed. The fringing effects from the outermost fingers will be accounted for using

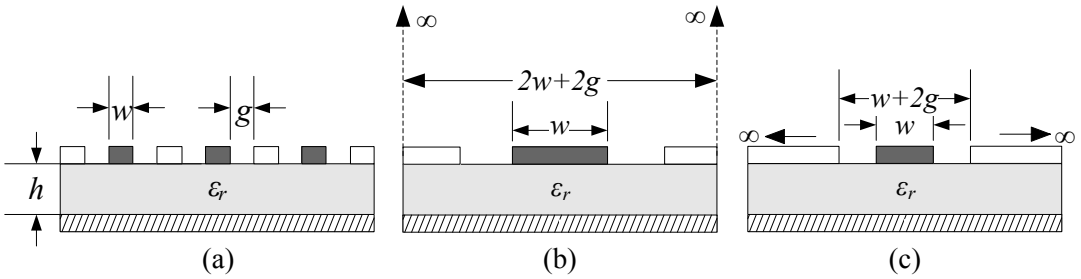

Fig. 2.3. Cross-sectional view of (a) CBICPW, (b) FWCBCPW in an infinite well, and (c) CBCPW with infinite width lateral conduction planes.

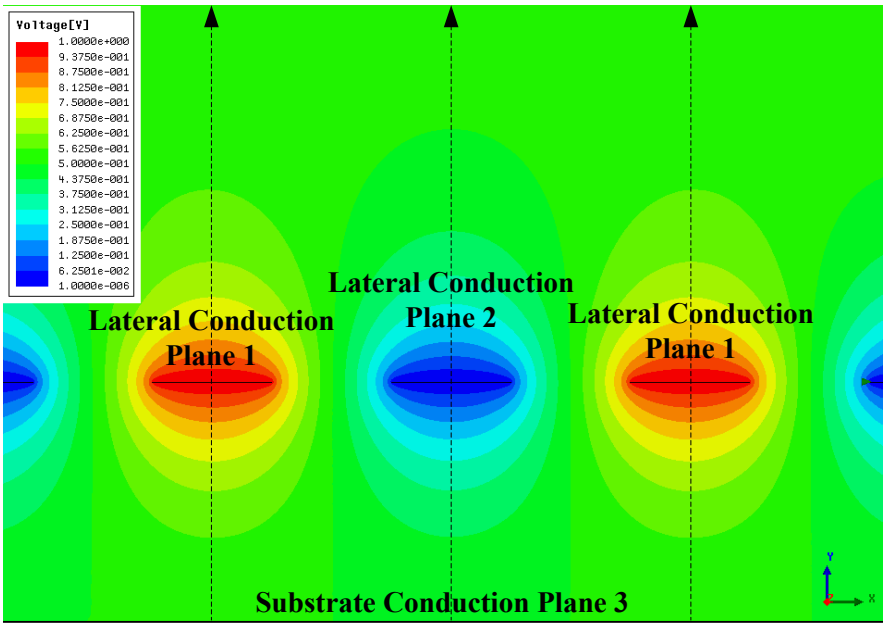

Fig. 2.4. Simulated potential distribution of the CBICPW cross section with magnetic walls inserted.

the derived effective length of the finger planes in the next section.

As previously mentioned in Chapter 1, the capacitance of the FWCBCPW in an infinite well has not been modeled due to its asymmetry. *Ghione et al.* has published a closed-form expression based on conformal mapping for the capacitance per unit length of a CBCPW with infinite-width conduction planes [14], however, with a cross-sectional view shown in Fig. 2.3(c). The total capacitance per unit length, C'_{∞}, is computed as the sum of the capacitance of the air above and the dielectric layer below the finger plane,

$$\begin{aligned} C'_{\infty} &= 2\varepsilon_0\left[\frac{K(k_0)}{K(k'_0)} + \varepsilon_r \frac{K(k_1)}{K(k'_1)}\right] \\ k_0 &= w/(w+2g) \\ k_1 &= \tanh(\pi w/4h)/\tanh(\pi(w+2g)/4h) \end{aligned} \tag{2.6}$$

where ε_0 is the permittivity of free space, w is the width of the line, g is the gap, h is the height of the interface dielectric, $K(k)$ is the complete elliptic integral of the first kind and $k'_i = \sqrt{1-k_i^2}$.

In a later publication [15], *Ghione et al.* proposed an adjustment for the capacitance per unit length due to the air in the upper half plane, C'_{air}, for finite-width lateral planes as seen in (2.7), though no adjustments could be found for the capacitance due to the dielectric in the lower half plane.

$$C'_{air} = 2\varepsilon_0 \left[2 \frac{K(k_0)}{K(k'_0)} \right]$$
$$k_0 = \frac{w}{(w+2g)} \sqrt{\frac{1-\left(\frac{w+2g}{3w+2g}\right)^2}{1-\left(\frac{w}{3w+2g}\right)^2}} \tag{2.7}$$

To estimate the change in capacitance of the lower half plane for finite-width lateral conduction planes, the CBCPW can be analyzed in terms of its hybrid-pi capacitance values. For small dielectric thicknesses, the majority of the interdigital capacitance is the contribution of the series capacitance between the upper conduction planes and the substrate conduction plane, $C_3/2$ in (2.8). The fringing capacitance, C_{12}, can be ignored during this case.

$$\lim_{h \to 0} C_{ID} = \frac{C_3}{2} \tag{2.8}$$

As the interface dielectric thickness approaches zero, the electric field lines emanate uniformly in the dielectric region, terminating on the substrate conduction plane similar to an ideal parallel plate capacitor. Consequently, the capacitance per unit length due to the dielectric in the lower half plane, C'_3, can be simply calculated by the width of the lateral conduction plane, w, over the height of the dielectric thickness, h. The total interdigital capacitance per unit length, C'_{ID}, can therefore be calculated as,

$$\lim_{h \to 0} C'_{ID} = \frac{C'_3}{2} = \varepsilon_0 \varepsilon_r \frac{w}{2h} \tag{2.9}$$

For infinite-width lateral conduction planes, the hybrid-pi capacitances are not symmetric. The interdigital capacitance per unit length is therefore expressed in its original form,

$$C'_{ID} = C'_{12} + \frac{C'_{13}\,C'_{23}}{C'_{13}+C'_{23}} = C'_{12} + \frac{1}{\frac{1}{C'_{13}} + \frac{1}{C'_{23}}} \tag{2.10}$$

Taking conduction plane 2 to be infinite, and therefore C'_{23} to be infinite as well, the interdigital capacitance per unit length, C'_{ID_∞}, can be expressed,

$$\lim_{h\to 0} C'_{ID\_\infty} = C'_{13} = \varepsilon_0 \varepsilon_r \frac{w}{h} \tag{2.11}$$

Using (2.9) and (2.11), the finite-width lateral conduction plane capacitance per unit length can be estimated as half that of the infinite lateral conduction plane,

$$C'_{ID} = \frac{C'_{ID\_\infty}}{2} \tag{2.12}$$

Therefore, (2.6) can be modified using (2.7) and (2.12) to estimate the total cross-sectional capacitance per unit length for finite-width lateral conduction planes leading to,

$$\begin{aligned} C' &= 2\varepsilon_0 \left[2\frac{K(k_0)}{K(k'_0)} + \frac{\varepsilon_r}{2}\frac{K(k_1)}{K(k'_1)} \right] \\ k_0 &= \frac{w}{(w+2g)} \sqrt{\frac{1-\left(\frac{w+2g}{3w+2g}\right)^2}{1-\left(\frac{w}{3w+2g}\right)^2}} \\ k_1 &= \tanh(\pi w/4h)/\tanh(\pi(w+2g)/4h) \end{aligned} \tag{2.13}$$

To verify the validity of the expression in (2.13), 2D field simulations were performed on the FWCBCPW in an infinite well in Ansoft MAXWELL™ for parameter values displayed in Table 2. Plots of the percentage error relative to the simulated data for both (2.13) and (2.9) are seen in Fig. 2.5. The gap dimensions used are small compared to the widths in order for the

Parameter	Value (μm)
w	50, 100, 150
g	5, 10, 20
h	0.25, 0.5, 1, 2, 5, 10,20, 30, 40, 50, 60, 70, 80, 100, 150, 200, 300

Table 2. Various device parameters used for 2D field simulation of FWCBCPW in an infinite well.

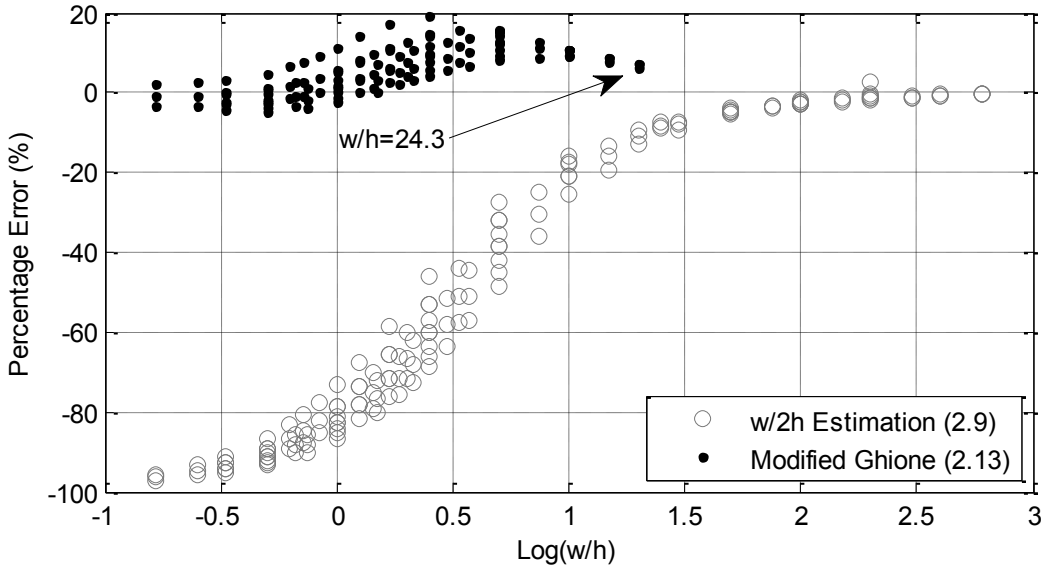

Fig. 2.5. Percentage error of the expressions in (2.9) and (2.13) to simulated data from MAXWELL™ with percentage error versus *w/h* for parameter values shown in Table 2.

infinite-width conduction plane estimation to hold true. Notwithstanding, the high error in Fig. 2.5 for (2.13) is the result of the gap becoming significant as compared to the finger width.

The parameter ratio *w/h* (finger width to dielectric thickness) is chosen for the *x*-axis to show the transition for the majority of the capacitance moving from the fringing capacitance, C'_{12}, to the series combination of the capacitance through the substrate conduction plane, $C'_3/2$. The *w/2h* estimation shows an estimation for $C'_3/2$ specifically, where at small *w/h* ratios the total capacitance is greatly underestimated. This underestimation is due to the fringing capacitance C'_{12} being the largest source of capacitance in the overall expression. As the *w/h*

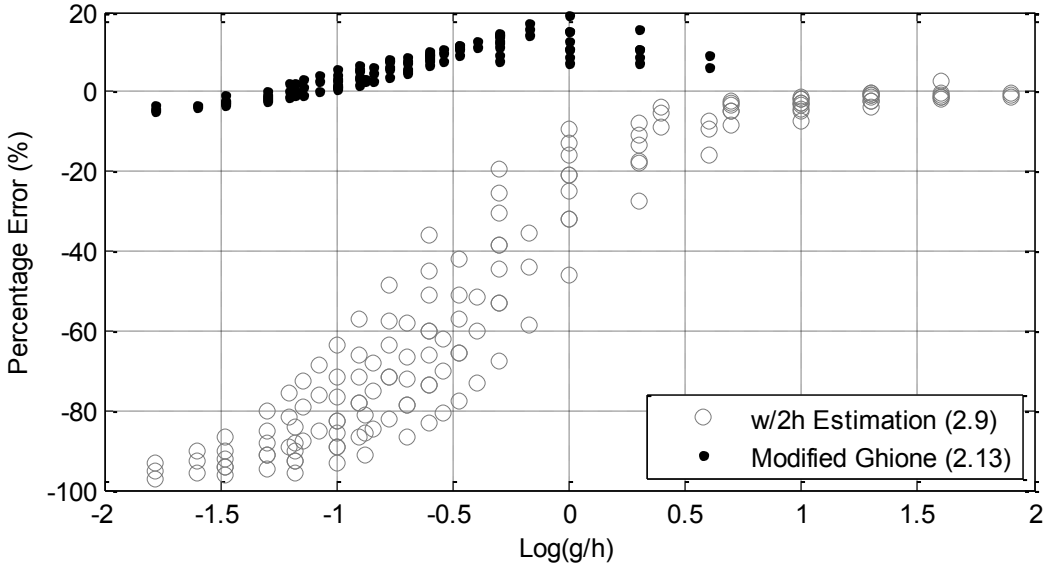

Fig. 2.6. Percentage error of the expressions in (2.9) and (2.13) to simulated data from MAXWELL™ with percentage error versus *g/h* for parameter values shown in Table 2.

ratio increases, the majority of the capacitance is due to C'_3 and the *w/2h* estimation becomes quite accurate.

To show the gap influence on the accuracy of the expressions, Fig. 2.6 plots percentage versus *g/h* (gap size to dielectric thickness). For the limiting case where the gap size is much larger than the dielectric thickness, $g/h \gg 1$, there is little fringing between the conductors. The electric field below the conductors is resultantly uniform, validating the *w/2h* estimation of the substrate coupling capacitance. For the dielectric thickness being much larger than the gap size, $g/h \ll 1$, the modified *Ghione* expression is most accurate due to the assumption made for a small gap size in (2.13) being validated. At the transition between these limiting cases, $g/h \sim 1$, the inaccuracy of the expression in (2.13) can be attributed to a significant amount of fringing capacitance where the gap size is not small compared to the finger width.

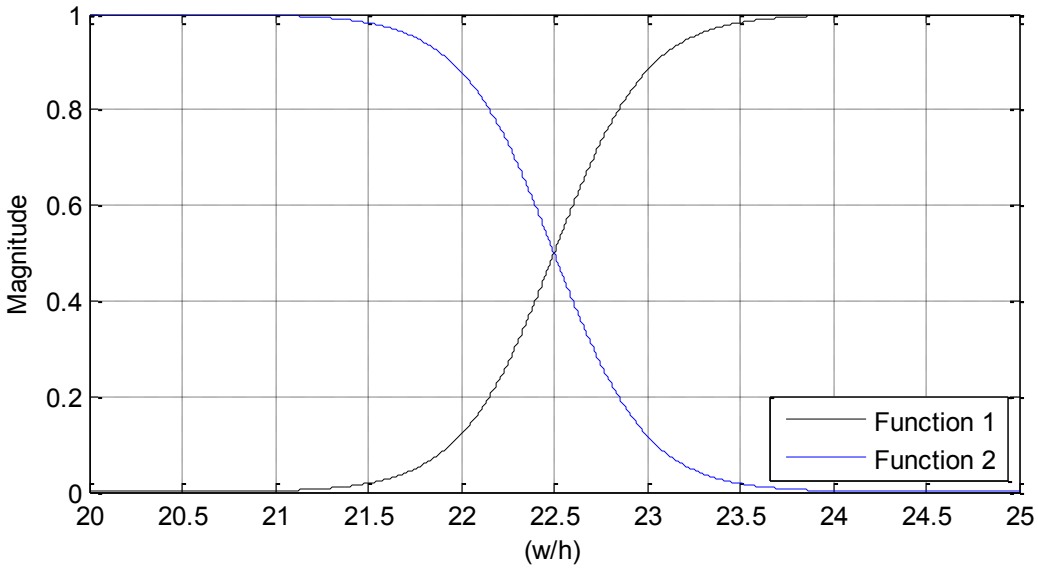

Fig. 2.7. Blending function used to allow continuous evaluation of the unit cell capacitance per unit length.

Also from the simulation results, Fig. 2.5, it can be seen that the expression in (2.13) is unable to be calculated at a *w/h* ratio greater than 24.3 using 64-bit double-precision floating-point variables. At this point, the ratio of hyperbolic tangents in the calculation of the parameter k_1 in (2.13) approaches unity and precision is lost. Fortunately, the estimation in (2.9) is reasonably valid, allowing for a continuous calculation of the cross-sectional capacitance, *C'*, on the unit cell using a blending function. The blending function chosen is plotted in Fig. 2.7 and the total capacitance is calculated as,

$$\begin{aligned} C' = 2\varepsilon_0 & \left[2\frac{K(k_0)}{K(k'_0)} + \frac{\varepsilon_r}{2}\frac{K(k_1)}{K(k'_1)} \right] \cdot \\ & \left[-\frac{1}{2}\tanh\left(2*\left(22.5 - \frac{w}{h} \right) \right) + \frac{1}{2} \right] \\ & + \varepsilon_0\varepsilon_r \frac{w}{2h}\left[\frac{1}{2}\tanh\left(2*\left(22.5 - \frac{w}{h} \right) \right) + \frac{1}{2} \right] \end{aligned} \tag{2.14}$$

where k_0 and k_1 are given in (2.13).

2.3 CBICPW Model Development

To obtain the total interdigital capacitance, the effective length of the interdigital fingers can be computed and used with the derived unit cell capacitance in (2.14). Two effective lengths are needed, one for the region using the modified *Ghione et al.* expression, and the other for the *w/2h* approximation. Assuming a uniform electric field, an approximation can be made for the capacitance of the CBICPW as the dielectric thickness approaches zero using the area of the finger planes over the thickness divided by two for the equal capacitance in series,

$$C = \varepsilon_0 \varepsilon_r \frac{(N/2)(l \cdot w) + w \cdot (N \cdot w + (N-1)g)}{2h} \tag{2.15}$$

where N is the number of fingers.

Factoring out a factor of *w/2h* results in an effective length, l_{eff_G23}, for the region of *w/h* greater than 24.3,

$$l_{eff\_G23} = N\left(g + w + \frac{l}{2}\right) - g \tag{2.16}$$

For the region of *w/h* less than 24.3, the general centerline length, *cl*, of the structure can be calculated,

$$cl = N(g + w + l) - l - \frac{3g}{2} \tag{2.17}$$

To arrive at an accurate effective length, 3D electromagnetic field simulations were performed in Ansoft MAXWELL™, pictured in Fig. 2.8, for finger lengths of 0.1, 5, 10, 15, 40, 75, 150, 200, and 350 µm with a finger width of 25 µm, gap size of 5 µm, and dielectric thicknesses ranging from 0.1 µm to 50 µm. Smaller simulations for finger width values ranging from 25 µm to 400 µm and gap size from 5 µm to 40 µm were also performed to more clearly

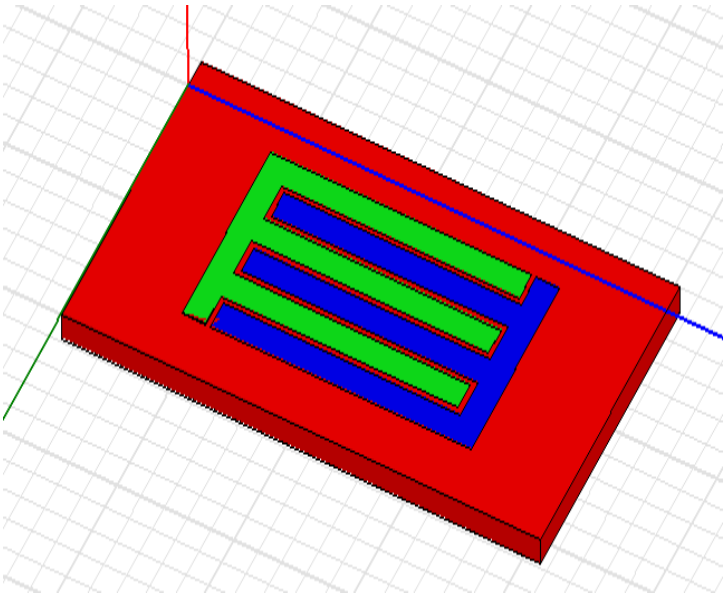

Fig. 2.8. Three dimensional model of CBICPW in MAXWELL™.

show their dependencies on the overall capacitance. With starting equations of (2.17) and (2.16), the effective length for small *w/h* was empirically determined to have the form of,

$$l_{eff\_L23} = a_0 \cdot N\left(g + w + \frac{l}{2}\right) - \frac{3g}{2} \tag{2.18}$$

where a_0 is an empirically derived coefficient. The coefficient a_0 was varied with percentage error calculations made using the simulated data set. A coefficient value was determined to minimize the mean error to the data set resulting in the effective length for small *w/h* to be,

$$l_{eff\_L23} = 0.839 \cdot N\left(g + w + \frac{l}{2}\right) - \frac{3g}{2} \tag{2.19}$$

Using (2.16) and (2.19) with (2.14), the resulting equation for the interdigital capacitance is expressed as

$$C_{ID} = C_{L23}\left[-\frac{1}{2}\tanh\left(2*\left(22.5-\frac{w}{h}\right)\right)+\frac{1}{2}\right]+C_{G23}\left[\frac{1}{2}\tanh\left(2*\left(22.5-\frac{w}{h}\right)\right)+\frac{1}{2}\right]$$

where

$$C_{L23} = 2\varepsilon_0\left[2\frac{K(k_0)}{K(k'_0)}+\frac{\varepsilon_r}{2}\frac{K(k_1)}{K(k'_1)}\right]\cdot\left[0.839\cdot N\left(g+w+\frac{l}{2}\right)-\frac{3g}{2}\right]$$

$$C_{G23} = \varepsilon_0\varepsilon_r\frac{w}{2h}\left[N\left(g+w+\frac{l}{2}\right)-g\right] \tag{2.20}$$

$$k_0 = \frac{w}{(w+2g)}\sqrt{\frac{1-\left(\frac{w+2g}{3w+2g}\right)^2}{1-\left(\frac{w}{3w+2g}\right)^2}}$$

$$k_1 = \tanh(\pi w/4h)/\tanh(\pi(w+2g)/4h)$$

Fig. 2.9 shows the percentage error for (2.15) and (2.20) to the simulated data samples of the CBICPW structure. The inset shows detail of the percentage error for small *w/h* where the three distinct lines are the result of three different gap sizes for varying the *w/h* ratio. For the

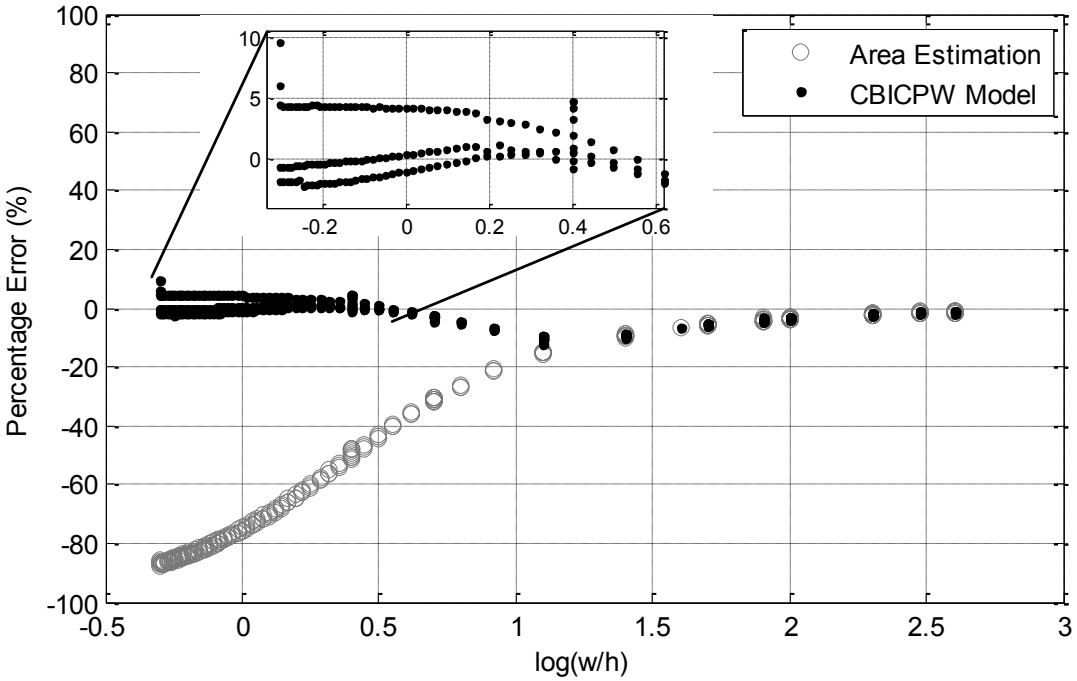

Fig. 2.9. Percentage error of the expressions in (2.15) and (2.20) to simulated CBICPW data from MAXWELL™.

expression in (2.20), the mean error is three percent to the simulated data, with a maximum of eleven percent at the transition between calculation regions. The relatively low percentage error across a wide range of input device parameters is demonstrated by the plot, specifically the wide range of dielectric thicknesses. The constraint of small gaps compared to finger widths is still a limitation placed upon the model. The best accuracy is obtained for either a large or small dielectric thickness as compared to the finger width and gap dimensions.

Chapter 3

CBICPW Measurements and Verification

In the previous chapter, the need for an analytical capacitance model for the CBICPW was addressed. This chapter seeks to verify the derived model with experimental evidence from fabricated structures. A brief overview of the fabrication of the CBICPW structures and the device dimensions is offered, followed by a derivation of the measurement theory. Finally, experimental results are presented and discussed in relation to the previously derived model.

3.1 CBICPW Device Fabrication

CBICPW structures were designed using layout tools within the Cadence environment. Structure layouts were sent to Corning, Inc. for fabrication on glass approximately 1 mm thick. The substrate and lateral conduction planes were formed with Aluminum, Al, and silicon

Parameter	Dimensional Value (μm)
N	6, 10, 50
w	4, 25, 100, 200
g	30, 50, 100
l	50,000, 1,000, 50
h	0.060, 0.192, 0.536

Table 3. Various device parameters for fabrication of CBICPW.

dioxide, SiO_2, was used for the interface dielectric. Five wafers were fabricated with varying dielectric thickness, although only three were usable for measurements. Table 3 displays the physical dimensions used for the structures.

The fabricated dielectric thicknesses are significantly smaller than the width and gap dimensions, indicating from Chapter 2 that the capacitive coupling through the substrate conduction plane constitutes the majority of the capacitance. A picture of the h=536 nm wafer can be seen in Fig. 3.1. To visualize the glass, a picture of a wafer without a dielectric interface or conductor backing is shown in Fig. 3.2. This second wafer was only utilized for experimental verification.

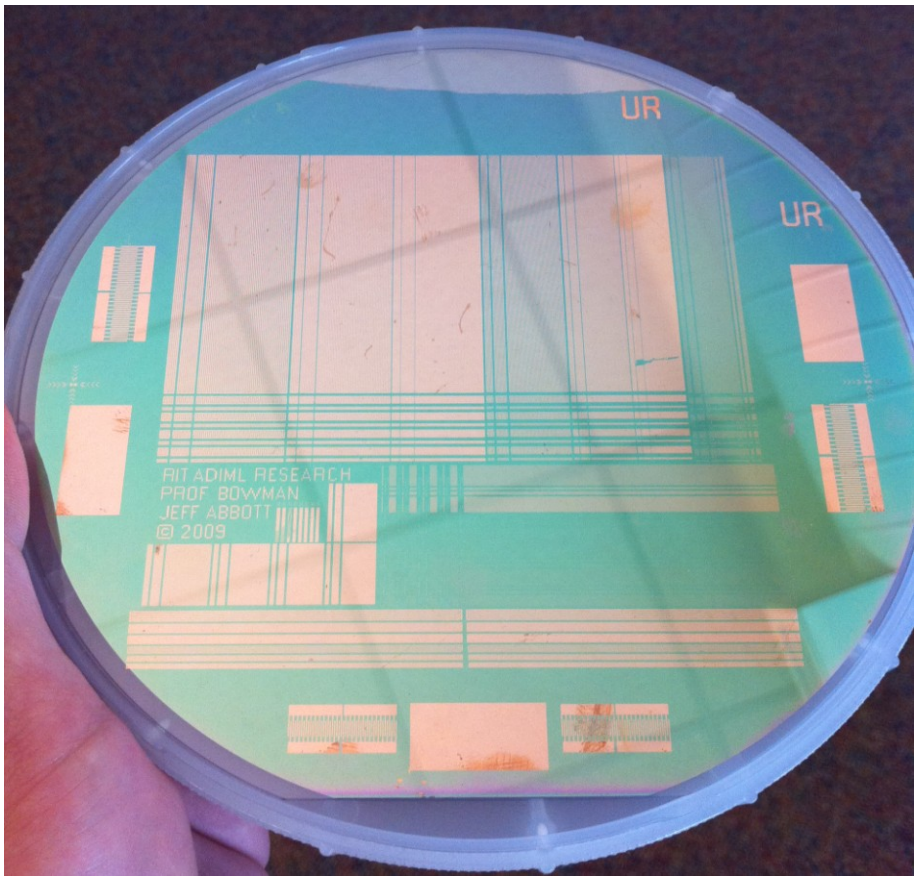

Fig. 3.1. Fabricated CBICPW 536 nm wafer on glass

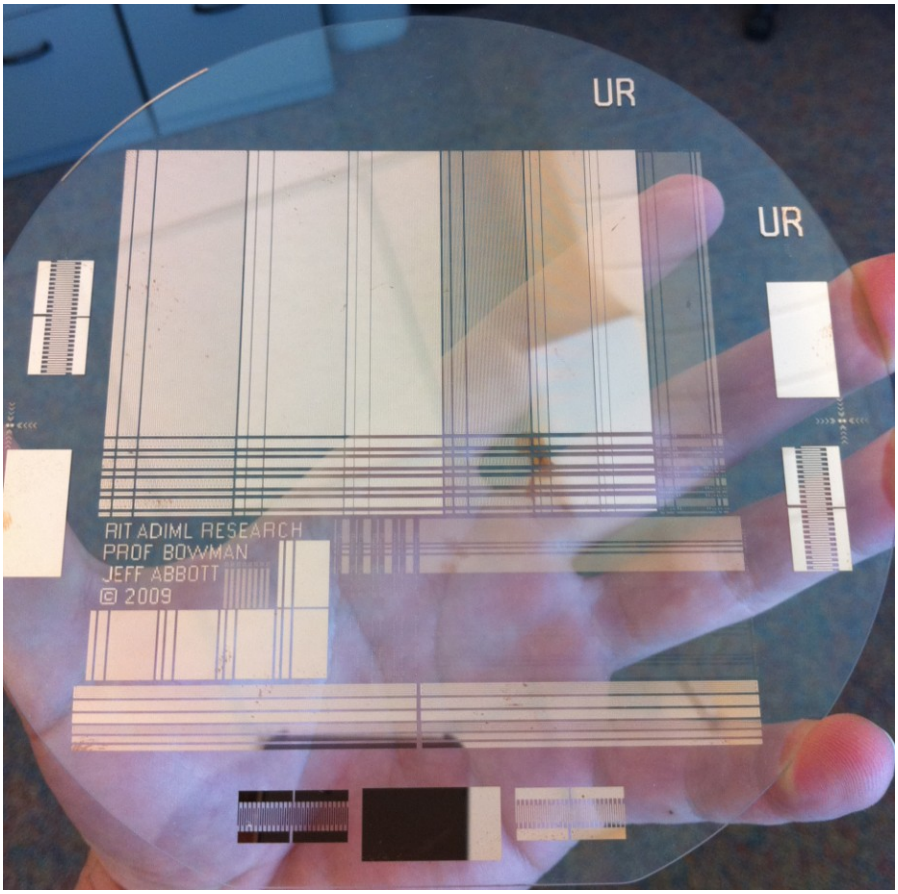

Fig. 3.2. IDC wafer on glass without conductor backing or dielectric interface.

3.2 Measurement Theory

The capacitance of the CBICPW structures were measured on an Agilent B1500A Semiconductor Device Analyzer. The capacitance measurement unit (CMU) in the B1500A uses a two-terminal nulling node technique for isolating the device under test (DUT) and accurately

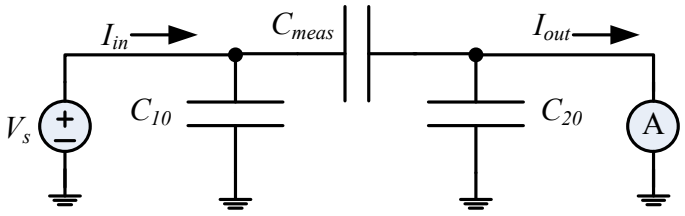

Fig. 3.3. Schematic representation of the CMU.

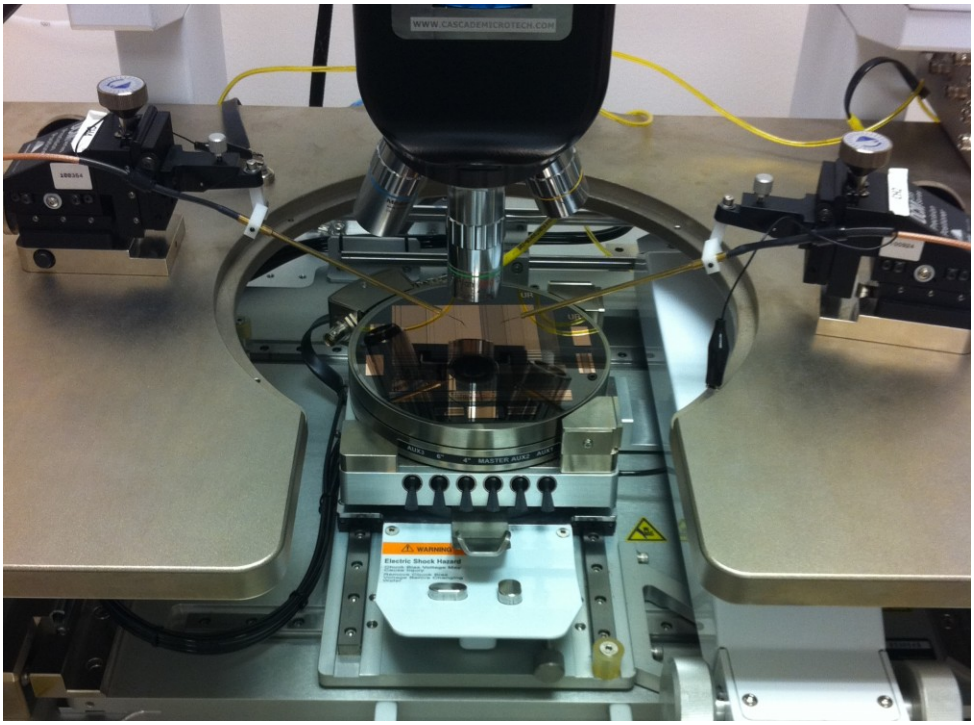

Fig. 3.4. Probe station used for capacitive measurements.

measuring the applied voltage and resultant current, represented in schematic form in Fig. 3.3. Voltage measurements are made on the input to the DUT and the current is measured by a transimpedance amplifier on the return path. With this configuration, parasitic capacitances, represented by C_{10} and C_{20}, are shorted to a small signal ground and do not affect the measurement.

A photograph of the Cascade Microtech high-frequency probe station used for the capacitive measurements is displayed in Fig. 3.4. A wafer with the test structures is placed on the chuck as shown in the middle of the photograph. Two dc point probes (brass arms), establish the actual connection to the test structure and are connected to the B1500A (not shown) using coaxial cables. A third coaxial cable connects the chuck to the B1500A's reference ground. The distributed parasitic capacitances from the coaxial leads are removed from the measurements by

performing open and short calibrations at the measuring frequency of 100 kHz. 100 μm by 100 μm probe pads were provided to contact minimum size test structure terminals.

The output current from the device in Fig. 3.3 can be expressed as,

$$I_{out} = \frac{V_s}{Z_{meas}} \tag{3.1}$$

where V_s is the applied voltage from the CMU, I_{out} is the output current, and Z_{meas} is the impedance of the measured capacitance. The measured impedance is therefore simply,

$$Z_{meas} = \frac{V_s}{I_{out}} \tag{3.2}$$

A schematic representation of the measurement system with the CBICPW hybrid-pi capacitance model is shown in Fig. 3.5. The additional capacitances C_{10}, C_{20}, and C_{30} represent parasitic capacitances and are referenced to ground. Similar to the previous case, the parasitic capacitances C_{10} and C_{20} are shorted to small signal ground with the applied voltage source and transimpedance amplifier on the return. However, a striking difference is the presence of a third terminal in the capacitive device structure under test. The capacitance C_{30} cannot be ignored and will induce a current (I_{loss}) to flow as the potential on the substrate conduction plane, V_x, is not

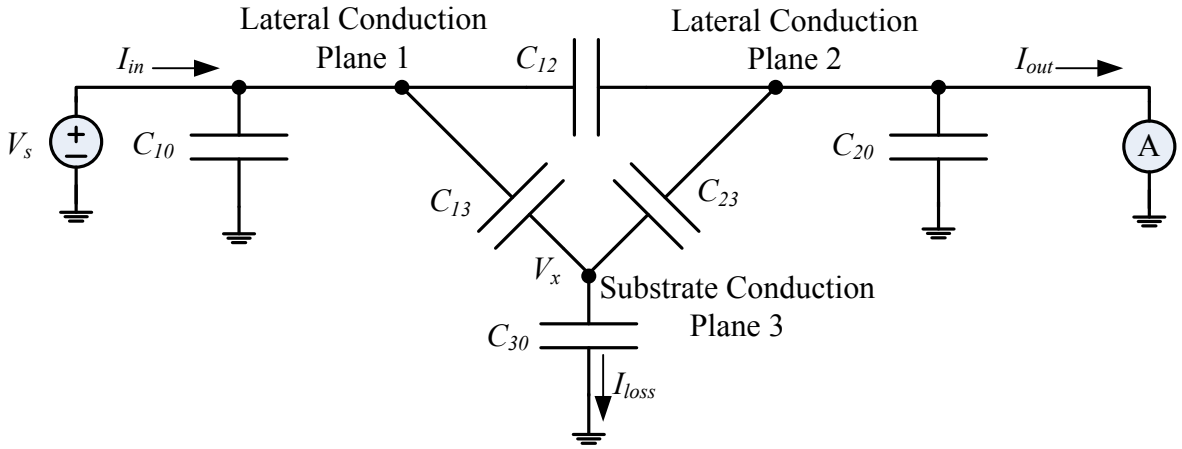

Fig. 3.5. Schematic representation of CMU with CBICPW hybrid-pi capacitance model.

fixed. With the capacitive coupling to the chuck on the probe station, this additional capacitance led to the misinterpretation of initial measurements. After verifying the measurement system with two terminal devices, the additional third terminal was included in the measurement theory to properly interpret the data.

From Chapter 2, it is expected that this voltage V_x will assume a value half that of the applied voltage V_s in order for the modeled capacitance to be measured. Performing nodal analysis at the unknown voltage, V_x, results in

$$V_x\left(\frac{1}{Z_{13}}+\frac{1}{Z_{23}}+\frac{1}{Z_{30}}\right)=\frac{V_S}{Z_{13}} \tag{3.3}$$

The expression in (3.3) can be simplified under the previous assumption that Z_{13} is equivalent to Z_{23} from the symmetry of the two finger planes and can be rewritten as Z_3,

$$V_x\left(\frac{2}{Z_3}+\frac{1}{Z_{30}}\right)=\frac{V_S}{Z_3} \tag{3.4}$$

Solving for V_x,

$$V_x=\frac{V_S}{\left(2+\frac{Z_3}{Z_{30}}\right)} \tag{3.5}$$

The current out of the device, I_{out}, can be expressed as

$$I_{out}=\frac{V_x}{Z_3}+\frac{V_s}{Z_{12}} \tag{3.6}$$

Substituting the measured current of (3.6) into the expression for measured impedance in (3.2),

$$Z_{meas}=\frac{V_s}{\frac{V_x}{Z_3}+\frac{V_s}{Z_{12}}}=\frac{V_sZ_3}{V_x+\frac{V_sZ_3}{Z_{12}}} \tag{3.7}$$

The expression in (3.5) may be combined with (3.7) to obtain an expression for the measured impedance, Z_{meas},

$$Z_{meas} = \frac{V_s Z_3}{\frac{V_S}{\left(2 + \frac{Z_3}{Z_{30}}\right)} + \frac{V_s Z_3}{Z_{12}}} = \frac{Z_3\left(2 + \frac{Z_3}{Z_{30}}\right)}{1 + \frac{Z_3}{Z_{12}}\left(2 + \frac{Z_3}{Z_{30}}\right)} \tag{3.8}$$

Substituting in capacitance values,

$$\frac{1}{C_{meas}} = \frac{\frac{1}{C_3}\left(2 + \frac{C_{30}}{C_3}\right)}{1 + \frac{C_{12}}{C_3}\left(2 + \frac{C_{30}}{C_3}\right)} = \frac{\left(2 + \frac{C_{30}}{C_3}\right)}{C_3 + C_{12}\left(2 + \frac{C_{30}}{C_3}\right)} \tag{3.9}$$

Solving for C_{meas} reduces (3.9) to

$$C_{meas} = C_{12} + \frac{C_3}{2 + \frac{C_{30}}{C_3}} \tag{3.10}$$

From this final form, the measured capacitance is smaller than expected for a significant parasitic capacitance on the substrate conduction plane. This loss of capacitance can be visualized by the I_{loss} current in Fig. 3.5. The potential, V_x, is also reduced from the expected $V_s/2$ by its coupling to ground for large C_{30},

$$V_x = \frac{V_S}{\left(2 + \frac{C_{30}}{C_3}\right)} \tag{3.11}$$

From Chapter 2, under the limiting case where the dielectric thickness approaches zero, resulting in C_3 being large compared to C_{12}, the total capacitance can be estimated using the area of the finger planes. With (3.10), this relationship can be used and expressed as,

$$\lim_{h\to 0} C_{meas} = \frac{C_3}{2} = C_{ID} \tag{3.12}$$

For smaller C_3 capacitance values, however, a reduction may not be made and C_{meas} can be solved for in terms of C_{ID} for C_{12} being insignificant,

$$C_{meas} = \frac{4C_{ID}^2}{4C_{ID} + C_{30}} \tag{3.13}$$

3.3 Measurement Results

To compare the derived model with measured data, both the interdigital capacitance, C_{ID}, and the parasitic capacitance on the substrate conduction plane, C_{30}, were measured and used in (3.13). To accurately characterize C_{30}, the chuck on which the fabricated wafers were placed was grounded, represented in Fig. 3.6. The parasitic capacitance could then be simply calculated as the capacitance between the substrate conduction plane through the glass dielectric to ground. The interface dielectric was etched away to expose the substrate conduction plane to allow measurement of the substrate conduction plane capacitance to ground. An insulator was placed between the glass and the grounded chuck to reduce the measured C_{30} capacitance from approximately 1 nF without the insulator to 38 pF with the insulator.

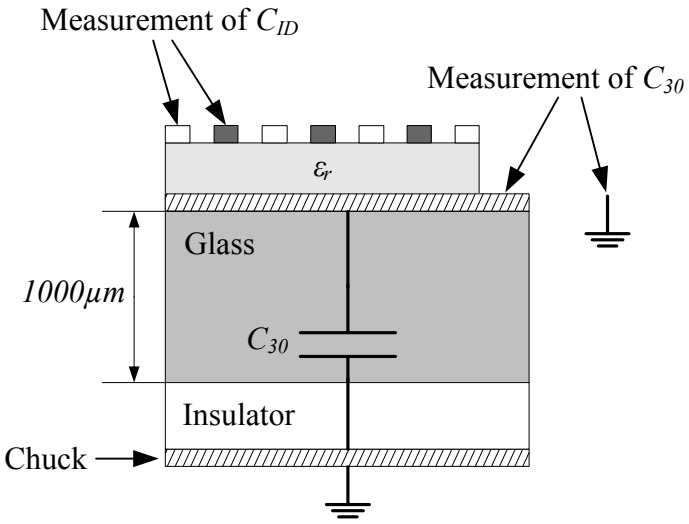

Fig. 3.6. Pictorial representation of measurements performed for C_{ID} and C_{30}.

With this value of 38 pF for C_{30}, the expression in (3.13) was experimentally seen to be valid for calculations using interdigital capacitance values above 7 pF. With smaller interdigital capacitance values, the contribution of C_{12} in (3.10) became significant, resulting in invalid calculations from (3.13). As noted, the two-terminal capacitance model assumed for the Agilent B1500A nulling measurement technique is not directly applicable for the CBICPW device structure. To compare laboratory measurements of CBICPW structures using a nulling node technique to a theoretical model for all capacitance values the individual hybrid-pi capacitances for the complete structure need to be considered.

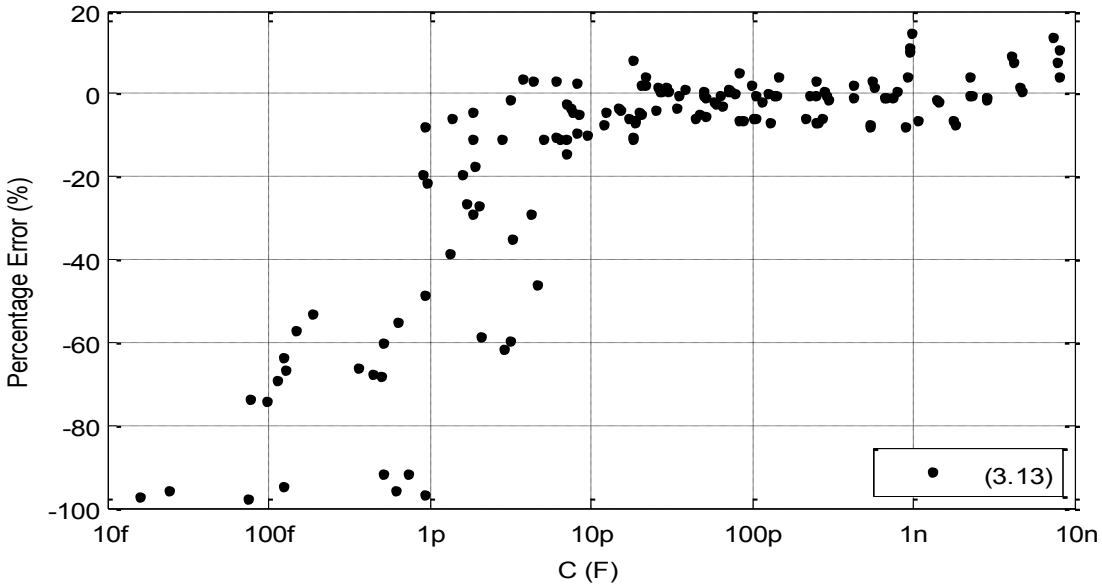

Fig. 3.7. Percentage difference of the expression in (3.13) to measured CBICPW data.

Fig. 3.7 displays the percentage difference of actual measured capacitance values to values calculated using (3.13). The difference for larger capacitance values can be described as process variation, shown by the corresponding normal distribution of error. For decreasing capacitance values, however, the measured capacitance is underestimated due to the contribution of C_{12} in (3.10) making the measured capacitance much larger than that predicted by (3.13). Overall, the capacitance values seen from the structures were mainly due to the series capacitance through the substrate conduction plane, with minimal fringing capacitance through either the dielectric layer or the air.

Chapter 4

Calculation of Elliptic Integrals Ratio

Conformal mapping has been a popular technique in solving electric field distributions due to its definition of preserving angles [39]. With this preservation of angles, two orthogonal families of curves lying on a region, such as electric field lines and equipotential lines, will remain orthogonal after being mapped to another region. A solution of Laplace's equation on the second region is therefore applicable to the first.

To demonstrate, if the mapping *w=f(z)* is an analytic function its derivative can be stated as [39],

$$\frac{dw}{dz} = f'(z) \tag{4.1}$$

and will not depend upon *dz* by definition. Writing *f'(z)* and *dz* in polar form,

$$f'(z) = M \cdot e^{j\mu}, \quad dz = ds \cdot e^{j\beta} \tag{4.2}$$

Equation (4.1) can therefore be solved for *dw*,

$$dw = f'(z) \cdot dz = M \cdot ds \cdot e^{j(\mu+\beta)} \tag{4.3}$$

From (4.3), the magnitude of *dw* is scaled by a factor *M* for any one point from the *z* plane. The magnitude *M* may change from point to point due to its functional dependence upon *z*.

Similarly, the direction of *dw* will be rotated by an angle μ that can vary from point to point as a function of *z*. As a result, the local angles at every point are preserved but can be rotated and scaled by μ and *M*, respectively, as determined by *f(z)*.

To validate the equivalence of Laplace's equation on both regions, Laplace's equation for the potential field, φ, is expressed using rectangular coordinates on the first region as,

$$\nabla^2 \cdot \phi = \frac{\partial^2 \phi}{\partial z_x^2} + \frac{\partial^2 \phi}{\partial z_y^2} = 0 \tag{4.4}$$

Using *f(w)*, the second order partial derivatives on the first region can be expressed in terms of those on the second [40],

$$\frac{\partial^2 \phi}{\partial z_x^2} + \frac{\partial^2 \phi}{\partial z_y^2} = \left| f'(z) \right|^2 \left(\frac{\partial^2 \phi}{\partial w_x^2} + \frac{\partial^2 \phi}{\partial w_y^2} \right) \tag{4.5}$$

Therefore, unless *f'(z)*=0, the vanishing of the left-hand side implies the vanishing of the parenthesis on the right [40], and vice versa.

4.1 Schwarz-Christoffel Mapping of Coplanar Striplines

The Schwarz-Christoffel transformation maps the real axis with points a_j onto the exterior of a simple polygon with points A_j and interior angles α_j, shown in (4.6) in differential form [36]. The upper half plane is correspondingly mapped to the interior of the polygon forming a bounded open region.

$$\begin{aligned}
&\frac{dz}{dw} = (w-a_1)^{\frac{-\alpha_1}{\pi}}(w-a_2)^{\frac{-\alpha_2}{\pi}}\ldots(w-a_n)^{\frac{-\alpha_n}{\pi}}, \quad z = f(w) \\
&\text{where} \\
&-\infty < a_1 < a_2 < \ldots < a_n < \infty \\
&-\pi \le \alpha_j \le 3\pi \quad (j = 1,2,\ldots,n), \quad -\pi \le \sum_{j=1}^{n} \alpha_j \le 3\pi, \quad \alpha_j \ne 0 \\
&A_j = f(a_j)
\end{aligned} \tag{4.6}$$

This mapping is ideal for solving the capacitance of two conductor planar structures. Placing the real axis along the common line of the conductors and assuming magnetic walls between the conductors, the problem can be split into the half plane regions above and below. A Schwarz-Christoffel conformal mapping of the upper half plane to a rectangular parallel plate configuration allows for an easy solution for the electric field and solution of the capacitance. A simple representation of this description is repeated from Chapter 1 in Fig. 4.1.

The mapping depicted in Fig. 4.1 can be expressed from (4.6) in integral form noting that

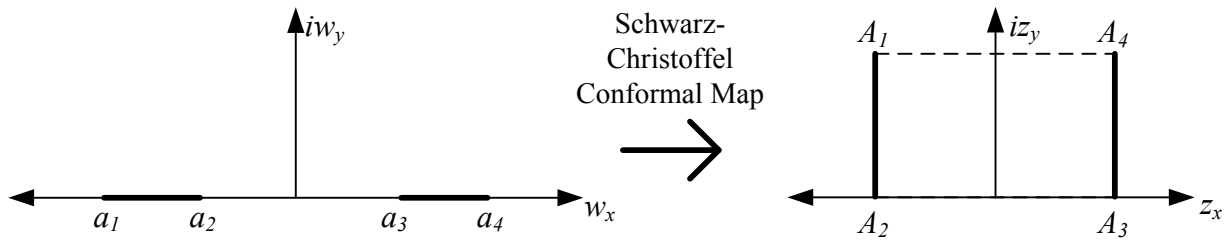

Fig. 4.1. Simple representation of a Schwarz-Christoffel transformation to a rectangular region.

the interior angles are $\pi/2$,

$$z = f(\omega) = \int_{\omega} \frac{dw}{\sqrt{(w-a_1)(w-a_2)(w-a_3)(w-a_4)}} \tag{4.7}$$

Liu published solutions for both asymmetric and symmetric conductors on the upper half plane and their corresponding electric field solutions based upon Schwarz-Christoffel conformal mappings [18]. Using a similar approach, a symmetric structure can be defined as in Fig. 4.2(a). The resultant mapping to a rectangular region, portrayed in Fig. 4.2(b), is expressed as,

$$z = f(\omega) = \int_0^{\omega} \frac{k \cdot dw}{\sqrt{(w^2-1)(k^2w^2-1)}} = k \cdot F\left(\text{asin}(\omega)\middle|k^2\right) \tag{4.8}$$

where F is the incomplete elliptic integral of the first kind and k is the modulus as defined in Fig. 4.2(a).

The points on the z-plane can be solved for by evaluating the points along the real axis,

$$\begin{aligned} f(-1/k)/k &= -K(k) + iK(k') \\ f(-1)/k &= -K(k) \\ f(1)/k &= K(k) \\ f(1/k)/k &= K(k) + iK(k') \end{aligned} \tag{4.9}$$

where $K(k)$ is the complete elliptic integral of the first kind evaluated using the modulus and $K(k')=K'(k)$ is the complement with $k' = \sqrt{1-k^2}$. The capacitance per unit length, C', is solved for by the width of the plates on the z-plane divided by the spacing between the plates [4][18].

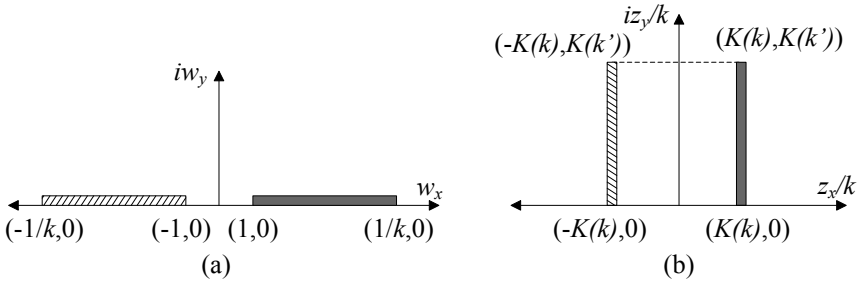

Fig. 4.2. Geometries of (a) two planar conductors on the upper half plane and (b) transformed conductors on the Schwarz-Christoffel rectangular region.

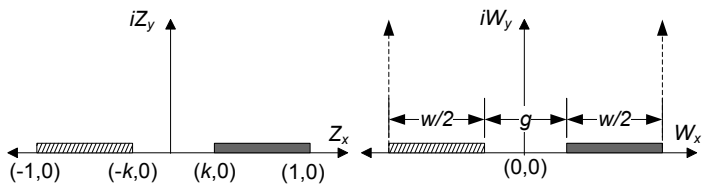

Fig. 4.3. Geometries of (a) CPS on the upper half-plane and (b) CPS in an infinite well.

$$C' = \varepsilon_0 \frac{K(k')}{2K(k)} \tag{4.10}$$

This formula is important for many applications. More elaborate geometries often map the conductors to the real axis and use similar Swartz-Christoffel transformations to map to a rectangular region. Consequently, many solutions of the capacitance, relative permittivity, and characteristic impedance often utilize this ratio with its inverse defined as the elliptic integrals ratio, *K/K'*.

A configuration that uses the solution is two coplanar striplines in an infinite well, seen in repeated structures such as the IDC. Fig. 4.3(a) shows a scaled version of Fig. 4.2(a), though it should be noted that the capacitance does not scale, with Fig. 4.3(b) displaying the coplanar striplines in an infinite well. To map the geometry from the infinite well to the configuration in Fig. 4.3(a), the mapping in (4.11) may be used with the capacitance per unit length, C'_{well}, being calculated in (4.12) [16].

$$Z = \sin\left(\frac{\pi \cdot W}{w+g}\right) \tag{4.11}$$

$$C'_{well} = \frac{\varepsilon_0}{2} \frac{K\left(\cos\left(\frac{\pi \cdot g}{2(w+g)}\right)\right)}{K\left(\sin\left(\frac{\pi \cdot g}{2(w+g)}\right)\right)} \tag{4.12}$$

4.2 Approximate Mapping of CPS using Simple Functions

The CPS in an infinite well may be defined on a semi-infinite strip plane *Z*, represented in Fig. 4.4(a) with points of interest defined in (4.13). The line segment $\overline{34}$ corresponds to an inserted conductor at the equipotential surface between the lateral conduction planes in Fig. 4.3(b) along the vertical axis.

$$Z_1 = 0, \quad Z_2 = i\frac{w}{2}, \quad Z_3 = i\left(\frac{g}{2}+\frac{w}{2}\right), \quad Z_4 = \infty + i\left(\frac{g}{2}+\frac{w}{2}\right), \quad Z_5 = \infty \tag{4.13}$$

A hyperbolic cosine function is used to map the outside of the semi-infinite strip to the real part of the *W* plane, depicted in Fig. 4.4 (b) and (4.14) [19].

$$W(Z) = \cosh\left(\frac{2\pi \cdot Z}{g+w}\right) - 1 \tag{4.14}$$

The points of interest on the *W* plane are calculated,

$$\begin{aligned} &W_1 = 0, \quad W_2 = -A, \quad W_3 = -2, \quad W_4 = -\infty, \quad W_5 = \infty \\ &\text{where} \\ &A = \cos\left(\frac{\pi \cdot g}{g+w}\right) + 1 \end{aligned} \tag{4.15}$$

The conductors are geometrically normalized on the *W* plane by multiplying by $1/\sqrt{2A}$ and are mapped symmetrically to the inside of the unit semi-circle using (4.16) and shown in Fig. 4.4(c). It is important to note that the open upper half-plane is mapped inside the unit circle creating a bounded region.

$$T(W) = \frac{i - \sqrt{\frac{W}{\sqrt{2A}}}}{i + \sqrt{\frac{W}{\sqrt{2A}}}} \tag{4.16}$$

The points of interest on the *T* plane are calculated and reduced,

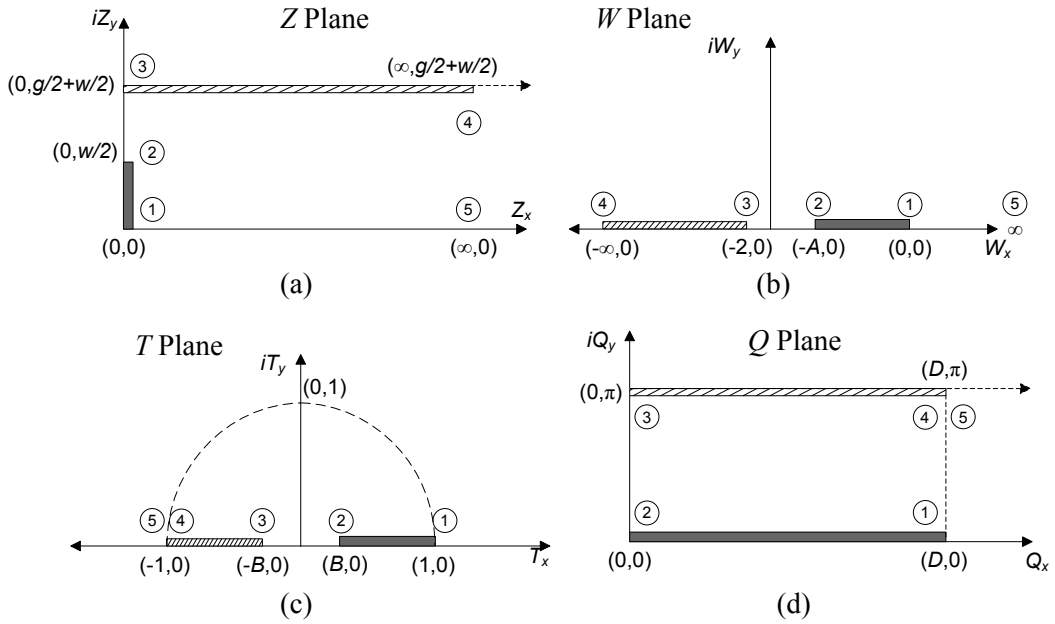

Fig. 4.4. Geometry for (a) CPS in an infinite well and the subsequent conformal mappings (b), (c), and (d).

$$T_1 = 1, \quad T_2 = B, \quad T_3 = -B, \quad T_4 = -1, \quad T_5 = -1$$

where

$$B = \frac{1 - \sqrt{\cos\left(\frac{\pi \cdot g}{2(g+w)}\right)}}{1 + \sqrt{\cos\left(\frac{\pi \cdot g}{2(g+w)}\right)}} \tag{4.17}$$

The inverse hyperbolic cosine function is found to approximate the inside of the unit semi-circle with a bounded rectangular region on a semi-infinite strip, Fig. 4.4(d) and (4.18).

$$Q(T) = \operatorname{acosh}\left(\frac{T}{B}\right) \tag{4.18}$$

The length of the conductors is calculated,

$$D = \operatorname{acosh}\left(\frac{1}{B}\right) \tag{4.19}$$

The capacitance per unit length is determined by the ratio of the length of the conductors and the height of the strip, shown in (4.20). The factor of 1/2 is the result of inserting the

conductor at the equipotential surface along the vertical axis in Fig. 4.3(b) to establish the structure in Fig. 4.4(a). The parameter q is defined as the inverse of B for convenience.

$$C' = \frac{\varepsilon_0}{2}\frac{\operatorname{acosh}(q)}{\pi}$$

where

$$q = \frac{1+\sqrt{\cos\left(\frac{\pi \cdot g}{2(g+w)}\right)}}{1-\sqrt{\cos\left(\frac{\pi \cdot g}{2(g+w)}\right)}} \tag{4.20}$$

A graphical depiction of the conformal mappings is displayed in Fig. 4.5 with equipotential surfaces for an equal width and gap. The gaps seen in the field for Fig. 4.5(b)-(d) would constitute the rest of the field on the Z plane, Fig. 4.5(a), which extends off to infinity.

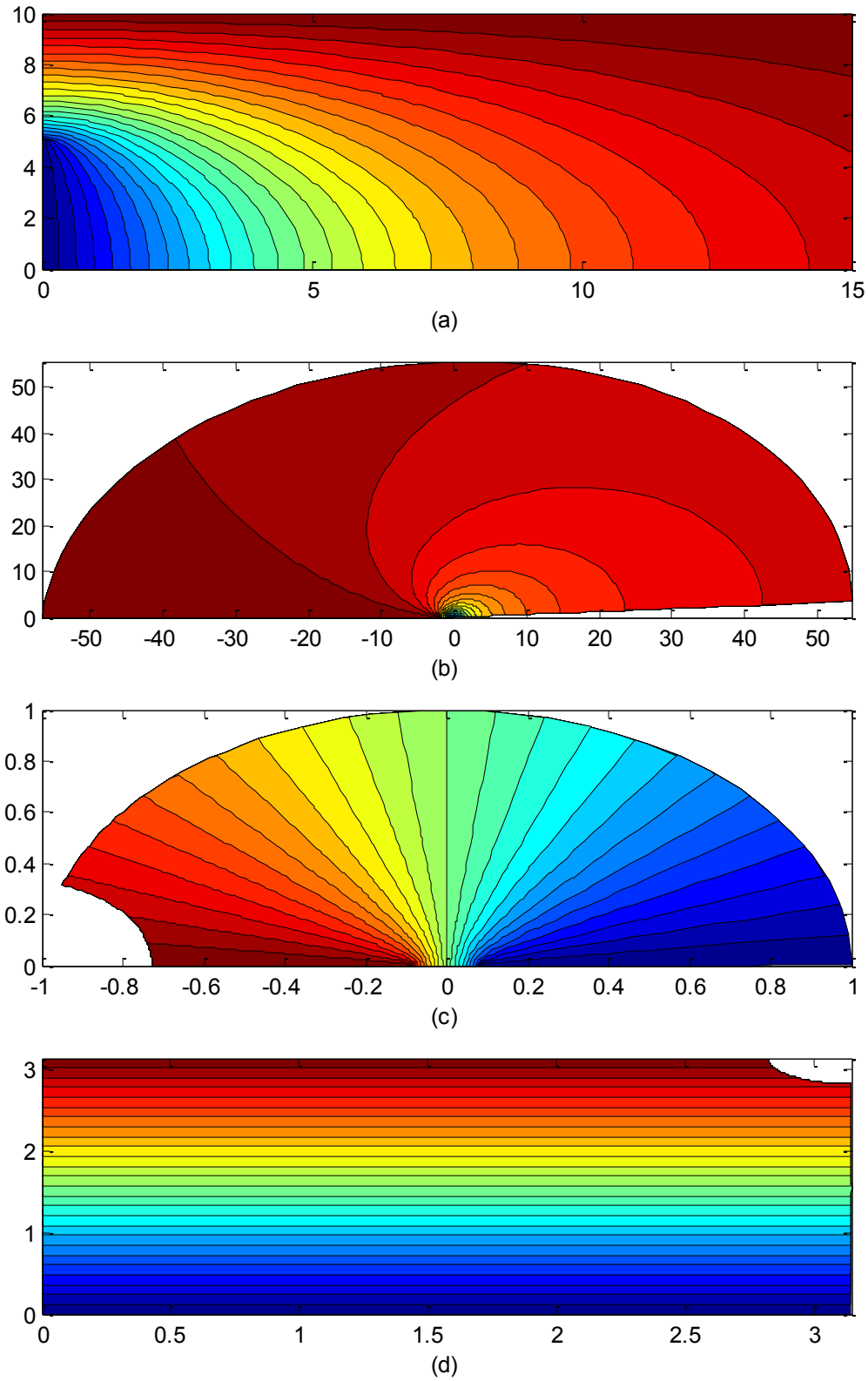

Fig. 4.5. Graphical depiction of simple conformal mappings showing equipotential surfaces on the (a) Z plane, (b) W plane, (c) T plane, and (d) Q plane.

4.3 Discussion of Approximation

The approximation of the mapping in (4.18) is assuming that the hyperbolic cosine function maps vertical lines on a horizontal semi-infinite strip to semi-circles on the positive upper half plane. Indeed, the hyperbolic cosine function maps vertical lines on a semi-infinite strip to catenary curves which approach constant curvature the further the vertical line is from zero on the semi-infinite strip. Consequently, the accuracy of the uniform field approximation is strictly dependent upon the width of the plates on the Q plane.

To account for the field not included in the mapping of the T plane to the Q plane, shown in Fig. 4.6(a) and Fig. 4.6(b), the area of the additional space is considered. For a rectangular region bounding a parallel plate configuration, the capacitance per unit length is proportional to the area of the region divided by the spacing between the two plates squared. Similarly, the capacitance on the Q plane can be estimated by the area of the bounded region divided by the width of the strip squared.

To estimate this area, the maximum real part of the curve on the Q plane, designated D_1, may be solved for using the real and complex parts of the hyperbolic cosine with the inverse of (4.18),

$$T(Q) = B\{\cos(Q_y)\cosh(Q_x) + i\sin(Q_y)\sinh(Q_x)\} \tag{4.21}$$

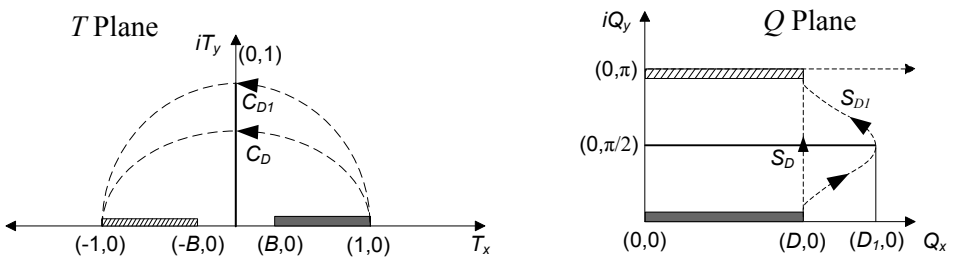

Fig. 4.6. Additional space considered with boundaries defined in the (a) T plane and (b) Q Plane.

The maximum on the Q plane, located at $D_1 + i\pi$, corresponds to the top of the unit semi-circle on the T plane, $0 + i$. Therefore, D_1 is solved for,

$$D_1 = \operatorname{asinh}\left(\frac{1}{B}\right) \tag{4.22}$$

The total area of the region is calculated as two trapezoids, with bases of D and D_1 and height $\pi/2$, and divided twice by π^2 to calculate the capacitance per unit length,

$$C' = \frac{\varepsilon_0}{2}\frac{\left[\operatorname{acosh}(q) + \operatorname{asinh}(q)\right]}{2\pi} \tag{4.23}$$

The expression in (4.23) can be simplified using a trigonometric identity,

$$C' = \frac{\varepsilon_0}{2}\frac{\operatorname{asinh}\left(q^2 + \sqrt{q^4 - 1}\right)}{2\pi} \tag{4.24}$$

4.4 Inspection of Iterative Function

Additional accuracy is obtained for calculating the capacitance per unit length in (4.24) by adding inverse hyperbolic cosine functions to the already derived expression of a similar form. Defining a function for the argument seen in (4.24),

$$f(q) = q^2 + \sqrt{q^4 - 1} = \exp\left(\operatorname{acosh}\left(q^2\right)\right) \tag{4.25}$$

an additional term may be averaged in,

$$C' = \frac{\varepsilon_0}{2}\frac{\left[\operatorname{asinh}\left(f(q)\right) + \operatorname{acosh}\left(f(q)\right)\right]}{4\pi} \tag{4.26}$$

Using the same trigonometric identity as used to simplify (4.23) to (4.24), (4.26) may be simplified to the form

$$C' = \frac{\varepsilon_0}{2}\frac{\left[\operatorname{asinh}\left(f\left(f\left(q\right)\right)\right)\right]}{4\pi} \tag{4.27}$$

A generic formulation can then be stated as,

$$C' = \frac{\varepsilon_0}{2}\frac{\left[\operatorname{asinh}\left(f_1\left(f_2\left(\ldots f_n\left(q\right)\ldots\right)\right)\right)\right]}{2^n\pi} \tag{4.28}$$

With growing iterations, the argument of the hyperbolic sine function increases significantly compared to unity with faster convergence obtained by approximating the hyperbolic function as a logarithm,

$$\operatorname{asinh}\left(x\right) = \ln\left(x + \sqrt{x^2+1}\right) \approx \ln\left(2x\right) \tag{4.29}$$

A final form for the capacitance per unit length of the CPS in an infinite well is expressed,

$$\begin{aligned} C'_{well} &= \frac{\varepsilon_0}{2}\frac{1}{\pi 2^n}\ln\left(2\cdot f_1\left(f_2\left(\ldots f_n\left(q\right)\ldots\right)\right)\right) \\ &\text{with} \\ f\left(q\right) &= q^2 + \sqrt{q^4-1} = \exp\left(\operatorname{acosh}\left(q^2\right)\right) \\ q &= \frac{1+\sqrt{\cos\left(\dfrac{\pi\cdot g}{2\left(g+w\right)}\right)}}{1-\sqrt{\cos\left(\dfrac{\pi\cdot g}{2\left(g+w\right)}\right)}} \end{aligned} \tag{4.30}$$

4.5 Calculation of Elliptic Integrals ratio

In previous work [37], the elliptic integrals ratio has been calculated as,

$$\begin{aligned}
&\frac{K(k)}{K(k')} = \frac{\pi}{\ln[2] + \ln\left[\frac{1+\sqrt{k'}}{1-\sqrt{k'}}\right]} \\
&for\ 0 < k \le 1/\sqrt{2} \\
&\frac{K(k)}{K(k')} = \frac{\ln[2] + \ln\left[\frac{1+\sqrt{k}}{1-\sqrt{k}}\right]}{\pi} \\
&for\ 1 > k \ge 1/\sqrt{2}
\end{aligned} \tag{4.31}$$

The symmetry in (4.31) is a byproduct of definitions from elliptic theory. As mentioned previously, the complement of the complete elliptic integral of the first kind, *K'(k)*, has the relationship with the complement of the elliptic modulus, *k'*,

$$K(k') = K'(k) \tag{4.32}$$

In addition, the definition of the elliptic modulus and its complement satisfies,

$$k^2 + k'^2 = 1 \tag{4.33}$$

Using (4.32) and (4.33), the elliptic integrals ratio can be manipulated to the form,

$$\frac{K(k)}{K'(k)} = \frac{K(k)}{K\left(\sqrt{1-k^2}\right)} = \frac{K\left(\sqrt{1-\sqrt{1-k^2}^2}\right)}{K\left(\sqrt{1-k^2}\right)} = \frac{K'(k')}{K(k')} \tag{4.34}$$

Defining a function, *ς(k)*, as an estimation of the elliptic integrals ratio,

$$\varsigma(k) \approx \frac{K(k)}{K'(k)} \tag{4.35}$$

A second calculation of the elliptic integrals ratio may be formed from (4.34),

$$\frac{K(k)}{K'(k)} \approx \frac{1}{\varsigma(k')} \tag{4.36}$$

For k ranging from 0 to $1/\sqrt{2}$, k' ranges from $1/\sqrt{2}$ to 1, as seen in (4.33). The symmetry about $1/\sqrt{2}$ in (4.31) is the result of the equivalent evaluation of the estimations of (4.35) and (4.36) at a value of $k'=k=1/\sqrt{2}$.

From the standard expression (4.12) and derived iterative expression (4.30), the elliptic integrals ratio may be solved for,

$$\begin{aligned}
&\frac{K(k)}{K(k')} = \lim_{n\to\infty} \frac{1}{\pi 2^n} \ln\left[2 \cdot f_1(f_2(\ldots f_n(q)\ldots))\right] \\
&\text{with} \\
&f(q) = q^2 + \sqrt{q^4 - 1} = \exp\left(\operatorname{acosh}\left(q^2\right)\right) \\
&q = \frac{1+\sqrt{k}}{1-\sqrt{k}}
\end{aligned} \tag{4.37}$$

Using (4.36), a second expression for the elliptic integrals ratio is solved,

$$\begin{aligned}
&\frac{K(k)}{K(k')} = \lim_{n\to\infty} \pi 2^n / \ln\left[2 \cdot f_1(f_2(\ldots f_n(q')\ldots))\right] \\
&\text{with} \\
&f(q) = q^2 + \sqrt{q^4 - 1} = \exp\left(\operatorname{acosh}\left(q^2\right)\right) \\
&q' = \frac{1+\sqrt{k'}}{1-\sqrt{k'}}
\end{aligned} \tag{4.38}$$

Fig. 4.7(a) and Fig. 4.7(b) illustrate a plot of the percentage error of the capacitance expression in (4.12) calculated using (4.37) and (4.38) for K/K', respectively. Results are displayed for four different values of n and for a conductor width-to-gap (w/g) ratio that spans over six orders of magnitude. MATLAB™'s built in function EllipKe is used as the reference for error calculations. The deviation from a smooth error curve for the calculations is attributed to convergence error bounds in the method of solution for the EllipKe function.

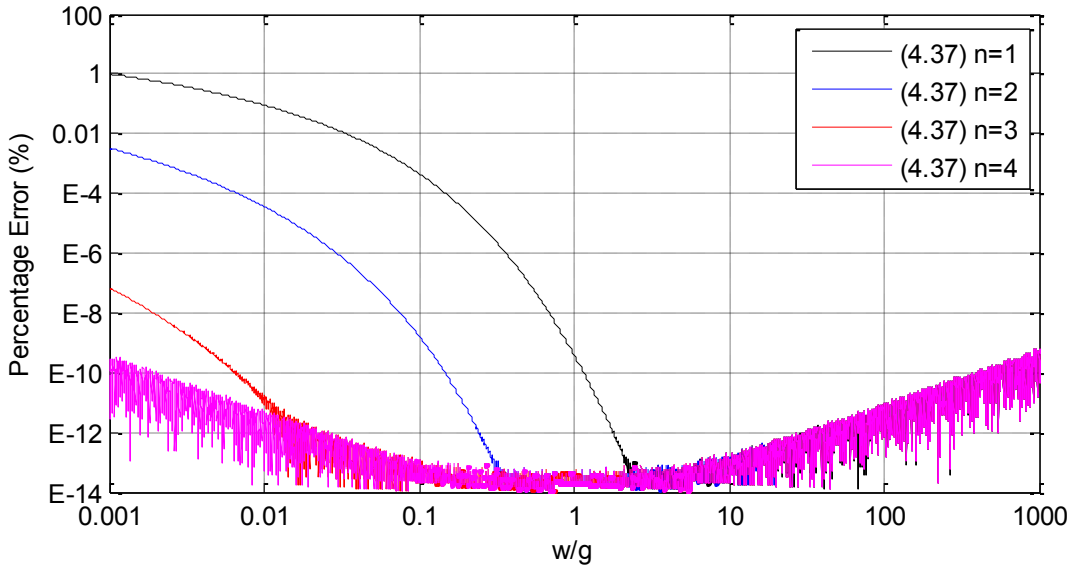

(a)

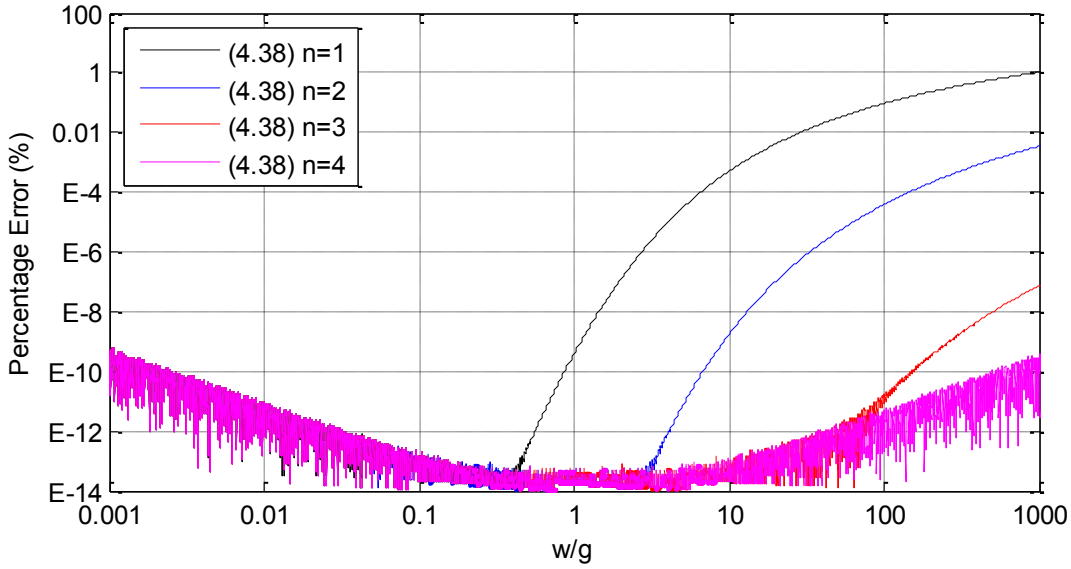

(b)

Fig. 4.7. Percentage error calculations of (4.12) using (a) (4.37) and (b) (4.38) using MATLAB™'s built in EllipKe function as a reference.

From the plots, it becomes clear that error is quickly driven out of the calculation with subsequent iterations. The symmetry of the two calculations about a *w/g* of unity is the result of $k=k'=1/\sqrt{2}$ at *w/g*=1.

A simple conditional evaluation expression can be formed for n=1 similar to (4.31) using the symmetry from (4.37) and (4.38),

$$\frac{K(k)}{K(k')} = \frac{\pi}{\ln[2] + \operatorname{acosh}\left[\left(\frac{1+\sqrt{k'}}{1-\sqrt{k'}}\right)^2\right]}$$
$$for\ 0 < k \le 1/\sqrt{2}$$
$$\frac{K(k)}{K(k')} = \frac{\ln[2] + \operatorname{acosh}\left[\left(\frac{1+\sqrt{k}}{1-\sqrt{k}}\right)^2\right]}{\pi} \tag{4.39}$$
$$for\ 1 > k \ge 1/\sqrt{2}$$

4.6 Calculation Comparisons

Fig. 4.8 shows a plot of the percentage error of the capacitance expression in (4.12) calculated using the standard expression (4.31), the derived conditional expression (4.39), and

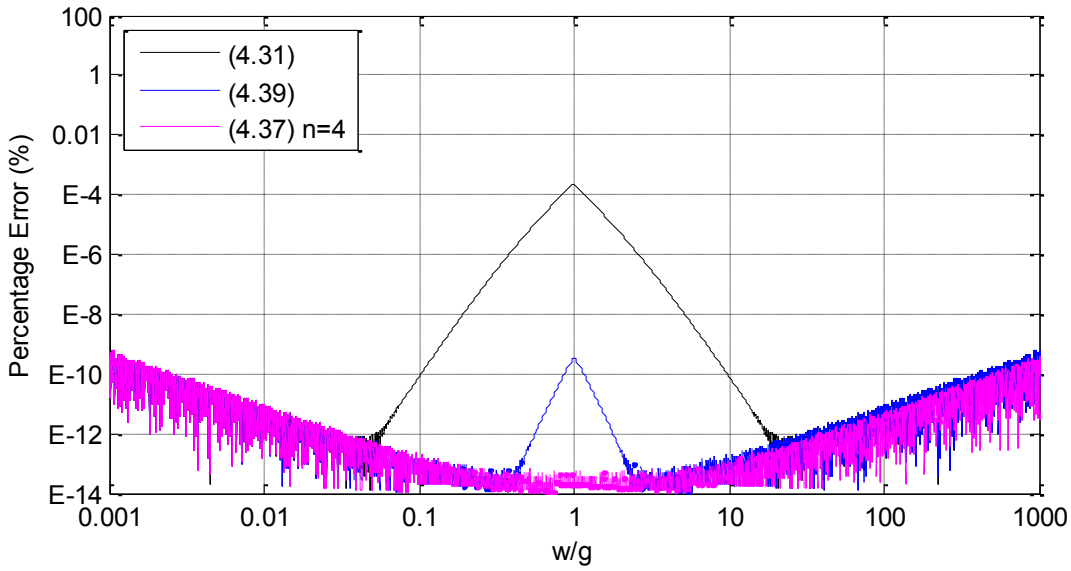

Fig. 4.8. Percentage error calculations of (4.12) using the standard expression (4.31), the derived conditional expression (4.39), and the derived iterative expression (4.37) using MATLAB™'s built in EllipKe function as a reference.

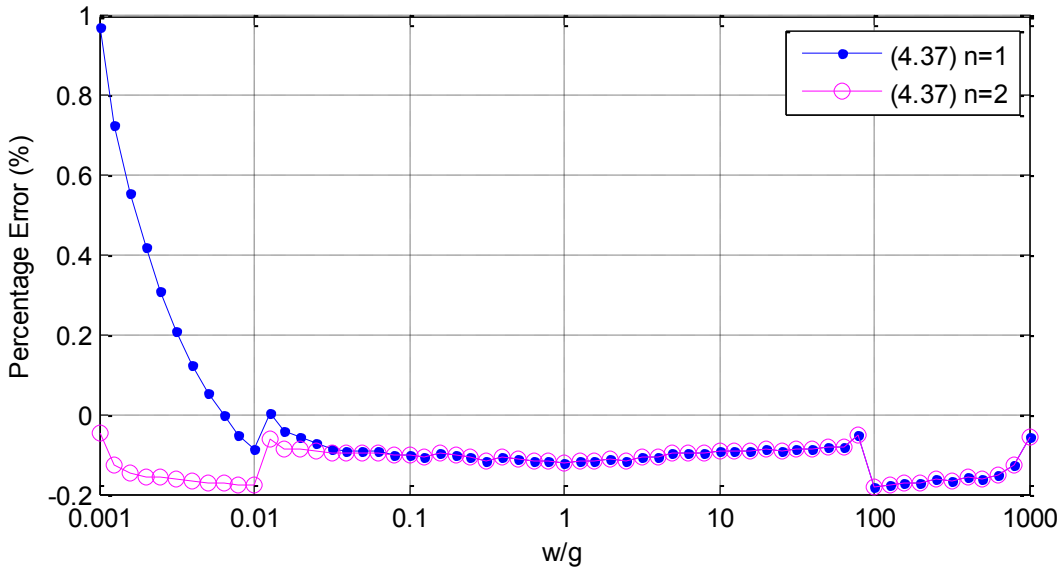

Fig. 4.9. Percentage error calculations of the derived iterative expression (4.37) to simulated data from MAXWELL™.

the derived iterative expression (4.37) with n=4 for calculating K/K'. The maximum error stated in *Hilberg*'s work [37], $3 \cdot 10^{-4}$ %, is seen at the peak of the error curve corresponding to a w/g=1 with good correspondence. The same region for k is used as defined from a w/g ratio spanning six orders of magnitude and MATLAB™'s built in function EllipKe is used as the reference for error calculations. The iterative solution in (4.37) provides the best results throughout the region without the need for a conditional statement for evaluation.

The calculation of capacitance in the derived iterative expression was compared to that of the commercial 2D field simulator MAXWELL™. The percentage error results are displayed in Fig. 4.9. As expected from Fig. 4.7(a), with n=1, about 1 % error is seen at a w/g ratio of one thousandth. Less than 0.2 % error is seen for (4.37) with n=2 and further iterations show no improvement due to the larger error bounds of the field simulator. The underestimation of capacitance evident in all simulations is attributed to the additional capacitance that is not

accounted for by the finite conductor thickness. The staircase effect is induced by adjusting the conductor thicknesses at *w/g* ratios of 0.01 and 100.

Chapter 5

Capacitive Modeling of FWCBCPW

The finite-width conductor-backed coplanar waveguide (FWCBCPW) in an infinite well is a specific geometry found in repeated planar structures with conductor backing. In doing research for modeling the CBICPW, it became apparent that no closed-form expressions were developed for the FWCBCPW due to its unique asymmetry in two dimensions. With the development of the closed-form expressions for the CPS in Chapter 4, similar approximate mappings can be used for the FWCBCPW, although with less precision. The derived expression is compared to simulated data using the MAXWELL™ field solver for a limited range of physical dimensions.

5.1 General Overview and Definitions

A cross-sectional view of the FWCBCPW in an infinite well is illustrated in Fig. 5.1 with

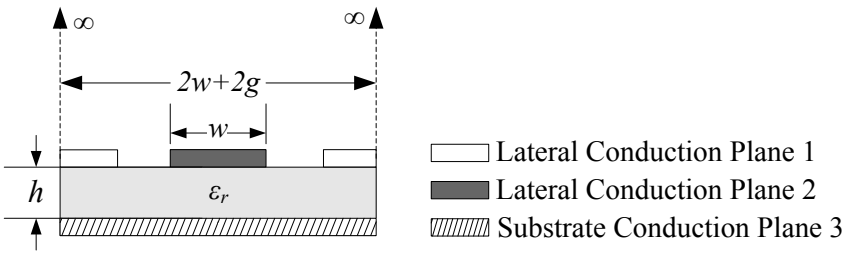

Fig. 5.1. Cross-sectional view of FWCBCPW in an infinite well.

the physical device parameters labeled. The height of the interface dielectric material is defined as h, the interface dielectric relative permittivity is ε_r, the width of the conductors is w, the spacing or gap between the conductors is g, and therefore the total width of the infinite well is $2w+2g$. For the three-conductor system, the charge exchange can be modeled using a hybrid-pi capacitance model,

$$\begin{bmatrix} Q'_1 \\ Q'_2 \\ Q'_3 \end{bmatrix} = \begin{bmatrix} C'_{12}+C'_3 & -C'_{12} & -C'_3 \\ -C'_{12} & C'_{12}+C'_3 & -C'_3 \\ -C'_3 & -C'_3 & 2C'_3 \end{bmatrix} \begin{bmatrix} V_1 \\ V_2 \\ V_3 \end{bmatrix} \tag{5.1}$$

where

$$C'_3 = C'_{13} = C'_{23}$$

where C'_{ij} is the hybrid-pi capacitance per unit length between conduction plane i and plane j, Q'_i is the charge per unit length on conduction plane i, and V_i is the potential of conduction plane i. The two lateral conduction planes are symmetric, resulting in the capacitances C'_{13} and C'_{23} being equivalent and simplified to C'_3.

To create symmetry for the field distribution, the substrate conduction plane is assumed floating with respect to an applied potential, V_o, across the lateral conduction planes, resulting in a potential vector,

$$V = \begin{bmatrix} V_o \\ 0 \\ 0.5 \cdot V_o \end{bmatrix} \tag{5.2}$$

The charge exchange, and therefore the modeled capacitance, is simply,

$$\begin{aligned} Q'_1 &= \left(C'_{12} + \frac{C'_3}{2} \right) \cdot V_o \\ Q'_2 &= -\left(C'_{12} + \frac{C'_3}{2} \right) \cdot V_o \\ Q'_3 &= 0 \end{aligned} \tag{5.3}$$

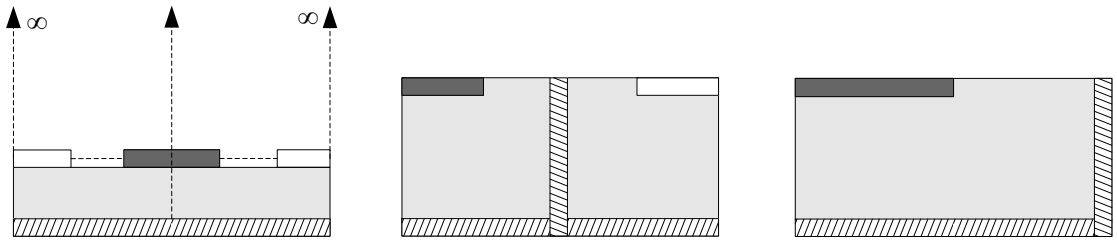

Fig. 5.2. Reduction of FWCBCPW to simpler geometries showing (a) inserted magnetic walls, (b) lower half quadrant with inserted conductor on the equipotential line, and (c) final reduced geometry.

From the symmetry of the applied potentials in (5.2), magnetic walls can be assumed, represented in Fig. 5.2(a) by dashed lines. The fields above and below the lateral conduction planes are isolated due to the horizontal magnetic walls and therefore can be solved independently. The capacitance of the field above is seen as the solution of two coplanar striplines in an infinite well with the expression (4.12) derived in Chapter 4. The field below the lateral conductors can be reduced by inserting a conductor along the equipotential line that exists between the two conductors, displayed in Fig. 5.2(b), to form a final geometry of Fig. 5.2(c).

5.2 Approximate Mapping of FWCBCPW using Simple Functions

The region below the lateral conduction planes may be modeled on the semi-infinite strip defined as the *Z* plane, depicted in Fig. 5.3(a) with points of interest defined in (5.4). The line segment $\overline{12}$ corresponds to the inserted conductor at the equipotential surface between the lateral conductor planes, $\overline{45}$ represents lateral conduction plane 1, and $\overline{23}$ is the substrate conduction plane 3.

$$Z_1 = 0, \quad Z_2 = ih, \quad Z_3 = \left(\frac{g}{2} + \frac{w}{2}\right) + ih, \quad Z_4 = \left(\frac{g}{2} + \frac{w}{2}\right), \quad Z_5 = \frac{g}{2} \tag{5.4}$$

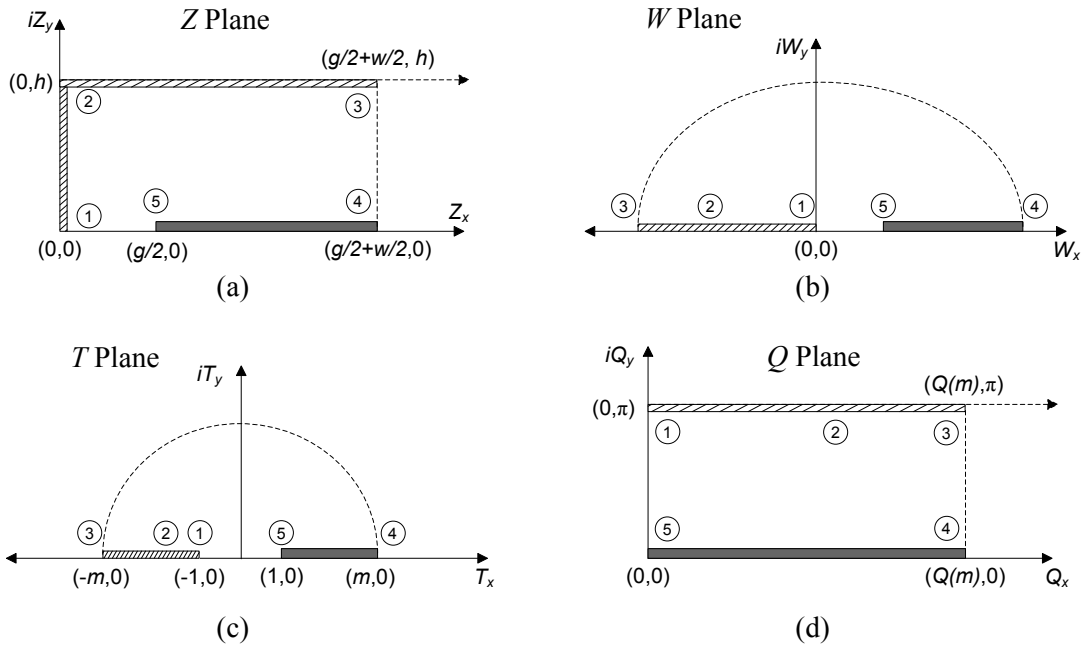

Fig. 5.3. Geometry for (a) FWCBCPW in an infinite well and the subsequent conformal mappings (b), (c), and (d).

Using a function similar to *Gevorgian et al.* [19], the outside of the semi-infinite strip Z is mapped onto the real axis of the W plane by the hyperbolic cosine, with the mapping displayed in Fig. 5.3(b),

$$W(Z) = \cosh\left(\frac{\pi \cdot Z}{h}\right) - 1 \tag{5.5}$$

The points of interest on the W plane are calculated,

$$\begin{aligned} &W_1 = 0, \quad W_2 = -2, \quad W_3 = -\cosh\left(\frac{\pi \cdot (w+g)}{2h}\right) - 1 \\ &W_4 = \cosh\left(\frac{\pi \cdot (w+g)}{2h}\right) - 1, \quad W_5 = \cosh\left(\frac{\pi \cdot g}{2h}\right) - 1 \end{aligned} \tag{5.6}$$

By applying a bilinear transformation, the two possibly asymmetrical conductors are mapped to conductors of equal width [18], expressed in Fig. 5.3(c) and (5.7).

$$T(W)=\frac{W+c_0}{\left(1+2\frac{c_0}{d}\right)\cdot W-c_0}$$

where

$$c_0=\begin{cases}\dfrac{-a(b+d)+\sqrt{ab(a+d)(b+d)}}{a-b}, & a\neq b\\ -d/2, & a=b\end{cases}$$

$$a=\cosh\left(\frac{\pi\cdot(w+g)}{2h}\right)+1$$

$$b=\cosh\left(\frac{\pi\cdot(w+g)}{2h}\right)-\cosh\left(\frac{\pi\cdot g}{2h}\right)$$

$$d=\cosh\left(\frac{\pi\cdot g}{2h}\right)-1 \tag{5.7}$$

The points of interest can be calculated on the *T* plane, seen in (5.8), with *m* being defined for convenience.

$$T_1=-1,\quad T_2=T(-2),\quad T_3=-m,\quad T_4=m,\quad T_5=1$$

where

$$m=\frac{-a+c_0}{-\left(1+2\frac{c_0}{d}\right)\cdot a-c_0} \tag{5.8}$$

From the *T* plane, an approximate mapping can be made to map the two conductors symmetrically to opposite sides of an infinite strip, shown in Fig. 5.3(d) and (5.9).

$$Q(T)=\operatorname{acosh}(T) \tag{5.9}$$

The points on the *Q* plane are calculated,

$$\begin{aligned}&Q_1=i\pi,\quad Q_2=Q(T(-2)),\\ &Q_3=Q(m)+i\pi,\quad Q_4=Q(m),\quad Q_5=0\end{aligned} \tag{5.10}$$

The capacitance per unit length of the dielectric region below the lateral conduction planes in Fig. 5.1, C'_{below}, is determined by the ratio of the length of the conductors and the height of the strip,

$$C'_{below} = \frac{\varepsilon_0 \varepsilon_r}{\pi} \operatorname{acosh}(m) \tag{5.11}$$

A graphical depiction of the conformal mappings is displayed in Fig. 5.4 with equipotential surfaces for w=g=h=1.

The total capacitance for the FWCBCPW in an infinite well can be calculated as the sum of the capacitance of the air, using (4.12), and dielectric, using (5.11),

$$C' = \varepsilon_0 \frac{K\left(\cos\left(\frac{\pi \cdot g}{2(w+g)}\right)\right)}{K\left(\sin\left(\frac{\pi \cdot g}{2(w+g)}\right)\right)} + \frac{\varepsilon_0 \varepsilon_r}{\pi} \operatorname{acosh}\left(\frac{a - c_0}{\left(1 + 2\frac{c_0}{d}\right) \cdot a + c_0}\right)$$

with

$$c_0 = \begin{cases} \dfrac{-a(b+d) + \sqrt{ab(a+d)(b+d)}}{a-b}, & a \neq b \\ -d/2, & a = b \end{cases} \tag{5.12}$$

$$a = \cosh\left(\frac{\pi \cdot (w+g)}{2h}\right) + 1$$

$$b = \cosh\left(\frac{\pi \cdot (w+g)}{2h}\right) - \cosh\left(\frac{\pi \cdot g}{2h}\right)$$

$$d = \cosh\left(\frac{\pi \cdot g}{2h}\right) - 1$$

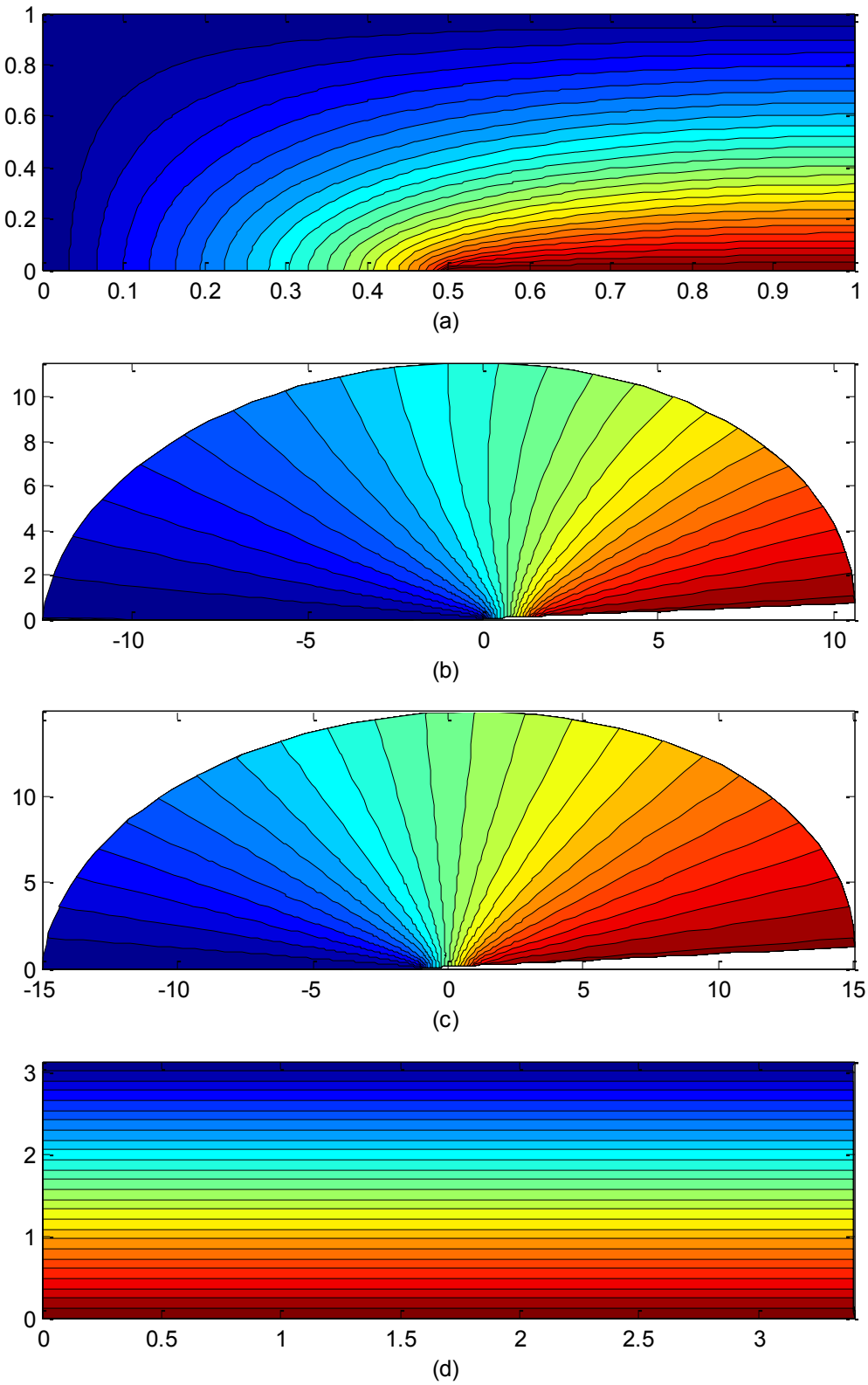

Fig. 5.4. Graphical depiction of simple conformal mappings showing equipotential surfaces on the (a) Z plane, (b) W plane, (c) T plane, and (d) Q plane.

5.3 Calculation Comparisons

The calculation of capacitance in the derived expression (5.12) was compared to that of the commercial 2D field simulator MAXWELL™. The device dimensions *w*, *g*, and *h* were each varied from 1 to 10 creating a 10x10x10 matrix of 1000 simulations. The percentage error results are displayed in Fig. 5.5. Fig. 5.5(a) shows the percentage error of (5.12) to the simulated data versus *h/g* on a semilog plot. Fig. 5.5(b) shows a three dimensional semilog plot of the percentage error versus the same *h/g* and, additionally, *w*. The widest variation in error is seen for small conductor widths with large gaps compared to the dielectric thickness. Using the rule of thumb where the substrate thickness should be twice that of the spacing or greater [4], the formula is seen to be approximately 3% accurate for the simulated set.

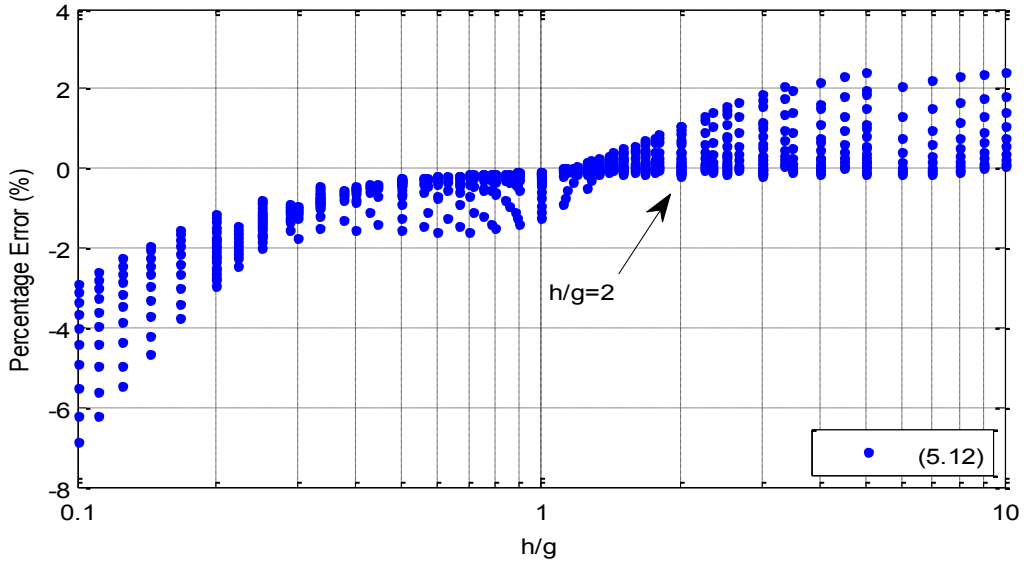

(a)

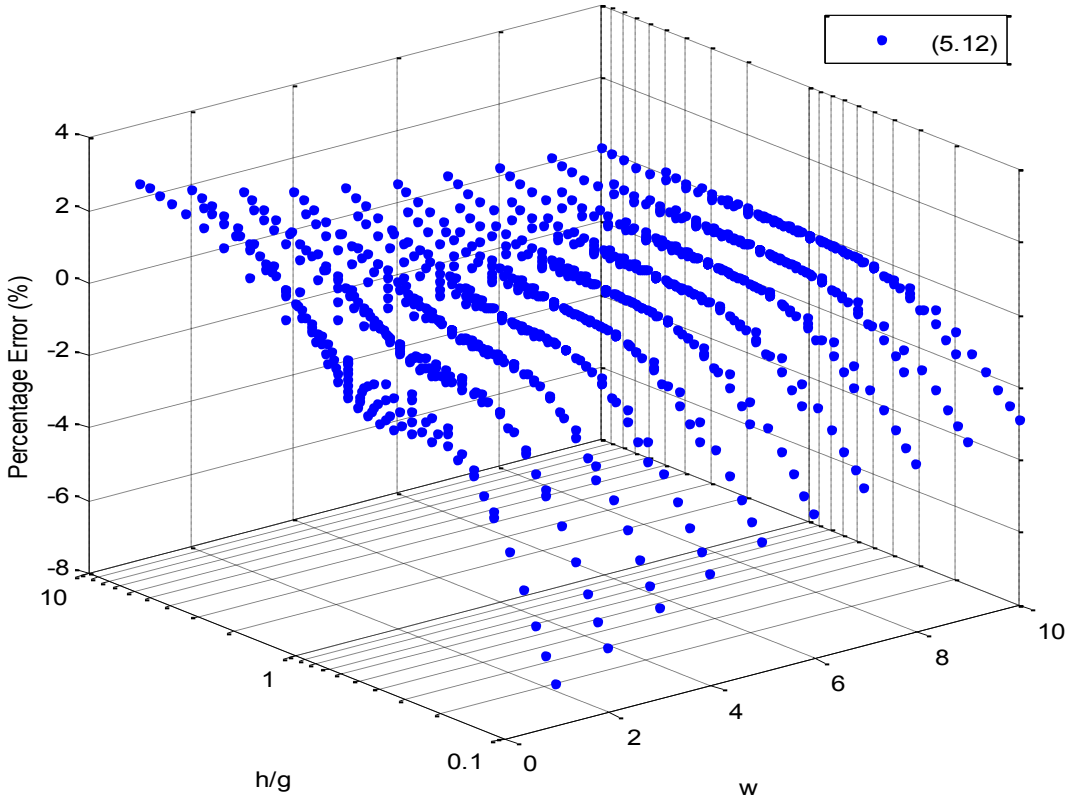

(b)

Fig. 5.5. Percentage error of the derived expression in (5.12) to simulated data from MAXWELL™ with (a) percentage error versus *h/g* and (b) percentage error versus *h/g* and *w*.

Chapter 6

Conclusions and Future Work

6.1 Conclusions

An efficient compact device model is presented for the conductor-backed interdigital coplanar waveguide with a broad range of flexibility for the interface dielectric thickness and other physical dimensions. Closed-form expressions were based on previous research for similar device structures with empirical variables directly extracted from data. A continuously differentiable interdigital capacitance expression was developed using only continuously differentiable expressions. The work extends previously developed expressions by *Ghione et al.* and provides a blending method for calculating capacitance where the *w/h* ratio exceeds 24, which is common for thin film dielectric structures. The modeled behavior compares well with a broad range of simulated and measured data with expressions developed to account for the loss of current through the substrate conduction plane during laboratory experiments.

Using simple function conformal mappings, a closed-form, iterative solution is derived for calculating the capacitance of the coplanar stripline. The new solution provides comparable accuracy to standard closed-form expressions using only simple functions. Capacitance

calculations from the solution are within 0.2 % of data from a commercial field solver for conductor width-to-gap ratios spanning six orders of magnitude. Based on the solution, a new continuously differentiable, iterative calculation technique for computing the elliptic integrals ratio demonstrates 10^{-11} relative error across a wide region.

The simple function conformal mappings for the CPS are extended to the finite-width conductor-backed coplanar waveguide in an infinite well to develop a closed-form solution for the capacitance. The new solution shows 7% accuracy to simulated data from a commercial field solver for device dimensions varied across an order of magnitude. For devices with a dielectric thickness which is twice that of the spacing, the resulting formula is 3% accurate for the simulated set.

6.2 Future Work

Future work for the CBICPW could extend into several areas. Using the traditional method of modeling the cross-sectional capacitance and adding in contributions from the finger ends and outermost fingers would eliminate the need for minimizing residuals to simulated data and offer a more physical interpretation of the overall capacitance. Modeling the individual hybrid-pi capacitance values through conformal mapping with different potentials would improve the usability of the model and allow the substrate to be set to a fixed potential rather than floating.

The measurement results and theory would also become more accurate with the hybrid-pi capacitances modeled, with the loss of current through the measurement system being able to be properly predicted. To compare measurements to theory more closely, physical dimensions that can be both simulated and fabricated could be utilized. Isolating the substrate conduction plane

for each individual structure would greatly reduce the parasitic capacitance to the substrate conduction plane and allow for accurate measurements of even small capacitance values.

The fast convergence of the iterative solution to the elliptic integrals ratio should be mathematically verified for convergence. If the solution converges, the theory could be applied to calculate the elliptic nome function, which in turn is used to calculate many elliptic integral functions. The theory could extend to the elliptic integrals in general and may offer new closed-form solutions. The relationship between the elliptic integrals ratio, the fast converging Landen transformation [37], and the iterative solution derived in this thesis could also provide insight into elliptic theory.

Modeling the FWCBCPW in an infinite well could be modified to include other mappings with special functions to provide more accurate results. Using an inverse Swartz-Christoffel mapping from the starting rectangular region to the real axis would eliminate the error seen and provide an exact solution. The base set of mappings could also be applied to similar structures for simple solutions of their capacitance.

6.3 Final Remarks

Characterizing physical structures with mathematical expressions has been a problem faced by engineers since the beginning of the profession. In order to predict and engineer the desired operation of a system, each subsequent level of complexity starting from the most basic must be analyzed and verified. Within this compilation of work, methods have been employed to address the need for mathematical interpretations of planar physical structures most commonly used by microwave engineers. With the growing developments of systems to come, the methods and

techniques explored could find their place in producing simple, efficient, and understandable expressions.

Bibliography

[1] K. C. Gupta, R. Garg, I. J. Bahl, and P. Bhartia, *Microstrip Lines and Slotlines*, 2nd ed.Artech House, Inc., 1996

[2] Houdart, M., "Coplanar Lines : Application to Broadband Microwave Integrated Circuits," *Microwave Conference, 1976. 6th European*, pp.49-53, 14-17 Sept. 1976

[3] Jackson, R.W., "Considerations in the Use of Coplanar Waveguide for Millimeter-Wave Integrated Circuits," *Microwave Theory and Techniques, IEEE Transactions on ,* vol.34, no.12, pp. 1450- 1456, Dec 1986

[4] Wen, C.P., "Coplanar Waveguide, a Surface Strip Transmission Line Suitable for Nonreciprocal Gyromagnetic Device Applications," *Microwave Symposium, 1969 G-MTT International* , pp.110-115, 5-7 May 1969

[5] O. G. Ramer, "Integrated optics electrooptic modulator electrode analysis," *J. Quantum Electron.*, vol. 18, pp. 386-392, Mar. 1982

[6] Special issue on "Application of lightwave technology to microwave devices, circuits and systems," *IEEE Trans. Microwave Theoy Tech.*, vol. 38, May 1990

[7] J. KeBler, R. Dill, and P. Russer, "Influence of buffer layers within YBCO coplanar waveguide structures," *IEEE Microwave and Guided Wave Letters*, vol. 2, Jan. 1992

[8] N. Newman and G. W. Lyons, "High-temperature superconducting microwave devices: Fundamental issues in materials, physics and engineering," *J. Supercond.*, vol. 6, no. 3, pp. 119-160, 1993

[9] H. Chung, W. S. C. Chang, and G. E. Bettes, "Microwave properties of travelling-wave electrodes in LiNbO:1 electrooptic modulators," *J. Lightwave Techno.*, vol. 1 I, pp. 1274-1278, Aug. 1993

[10] Chen-Cheng Wang, Chi-Hui Lai, Tzyh-Ghuang Ma, "Novel uniplanar synthesized coplanar waveguide and the application to miniaturized rat-race coupler," Microwave Symposium Digest (MTT), *2010 IEEE MTT-S International*, pp.708-711, 23-28 May 2010

[11] Gui Wang, Rushan Chen, Wanchun Tang, "Analysis and implementation of MEMS coplanar waveguide on silicon substrate," *Microwave and Millimeter Wave Technology (ICMMT), 2010 International Conference on ,* pp.2071-2074, 8-11 May 2010

[12] Chris Nassar, Carlo Kosik-Williams, Dave Dawson-Elli, Robert J. Bowman, Single Fermi Level, "*Thin Film CMOS on Glass: The Behavior of Enhancement Mode PMOSFETs from Cutoff through Accumulation*", IEEE Transactions on Electron Devices, September, 2009

[13] Cheng, K.K.M., Everard, J.K.A., "A new technique for the quasi-TEM analysis of conductor-backed coplanar waveguide structures," *Microwave Theory and Techniques, IEEE Transactions on ,* vol.41, no.9, pp.1589-1592, Sep 1993

[14] Ghione, G., Naldi, C., "Parameters of coplanar waveguides with lower ground plane," *Electronics Letters*, vol.19, no.18, pp.734-735, September 1 1983

[15] Ghione, G., Naldi, C.U., "Coplanar Waveguides for MMIC Applications: Effect of Upper Shielding, Conductor Backing, Finite-Extent Ground Planes, and Line-to-Line Coupling," *Microwave Theory and Techniques, IEEE Transactions on ,* vol.35, no.3, pp. 260-267, Mar 1987

[16] R. Igreja and C. J. Dias, "Analytical evaluation of the interdigital electrodes capacitance for a multi-layered structure," *Sens. Actuators*, vol. 112, pp. 291–301, 2004

[17] Gevorgian, S., Linner, L.J.P., Kollberg, E.L., "CAD models for shielded multilayered CPW," *Microwave Theory and Techniques, IEEE Transactions on ,* vol.43, no.4, pp.772-779, Apr 1995

[18] T. K. Liu, "Impedances and field distributions of two coplanar parallel perfectly conducting strips with arbitrary widths," AFWL Interaction notes, note 182, Jul. 1974

[19] Gevorgian, S.S., Martinsson, T., Linner, P.L.J., Kollberg, E.L., "CAD models for multilayered substrate interdigital capacitors," *Microwave Theory and Techniques, IEEE Transactions on ,* vol.44, no.6, pp.896-904, Jun 1996

[20] Zhu, N.H., Pun, E.Y.B., Chung, P.S., "Field distributions in supported coplanar lines using conformal mapping techniques," *Microwave Theory and Techniques, IEEE Transactions on ,* vol.44, no.8, pp.1493-1496, Aug 1996

[21] Carlsson, E., Gevorgian, S., "Conformal mapping of the field and charge distributions in multilayered substrate CPWs," *Microwave Theory and Techniques, IEEE Transactions on ,* vol.47, no.8, pp.1544-1552, Aug 1999

[22] Jae-Woong Lee, Ic-Pyo Hong, Tae-Hoon Yoo, Han-Kyu Park, "Quasi-static analysis of conductor-backed coupled coplanar waveguide," *Electronics Letters*, vol.34, no.19, pp.1861-1862, 17 Sep 1998

[23] Gevorgian, S., Carlsson, E., Rudner, S., Wernlund, L.-D., Wang, X., Helmersson, U., "Modelling of thin-film HTS/ferroelectric interdigital capacitors ," *Microwaves, Antennas and Propagation, IEE Proceedings* - , vol.143, no.5, pp.397-401, Oct 1996

[24] C. Veyers and V. F. Hanna, "Extension of the application of conformal mapping techniques to coplanar lines with finite dimensions," *Int. J. Electron.*, vol. 48, pp. 47-56, Jan. 1980

[25] S. Visan, O. Picon, V. Fouad Hanna, "3D characterization of air bridges and via holes in conductor-backed coplanar waveguides for MMIC applications," *Microwave Symposium Digest, 1993., IEEE MTT-S International* , vol., no., pp.709-712 vol.2, 1993

[26] Jinchang Zhao, Yu Tian, Yan Chen, Bo Gao, Ling Tong, "The analysis of electromagnetic characteristics of coplanar waveguide in different models using Finite-Difference Time-Domain method," Microwave and Millimeter Wave Technology, 2008. ICMMT 2008

[27] Ma, Z., Yamashita, E., "Comparative studies of discontinuities in single and double layered conductor-backed coplanar waveguides," *Microwave Symposium Digest, 1996., IEEE MTT-S International*, vol.3, pp.1803-1806 vol.3, 17-21 Jun 1996

[28] Thompson, D.A., Rogers, R.L., "The interdigital coplanar waveguide: a new low-impedance micromachinable planar structure," *Microwave and Guided Wave Letters, IEEE*, vol.8, no.7, pp.257-259, Jul 1998

[29] Yaozhong Liu, Itoh, T., "Control of leakage in multilayered conductor-backed coplanar structures," *Microwave Symposium Digest, 1994., IEEE MTT-S International*, pp.141-144 vol.1, 23-27 May 1994

[30] Knorr, J.B., Kuchler, K., "Analysis of Coupled Slots and Coplanar Strips on Dielectric Substrate," *Microwave Theory and Techniques, IEEE Transactions on ,* vol.23, no.7, pp. 541- 548, Jul 1975

[31] Elkordy, M., "Analysis of Conductor-Backed Coplanar Waveguide using Integral Method," *Communications and Information Technologies, 2006. ISCIT '06. International Symposium on ,* pp.787-790, Oct. 18 2006-Sept. 20 2006

[32] Yamashita, E., Atsuki, K., "Analysis of Microstrip-Like Transmission Lines by Nonuniform Discretization of Integral Equations," *Microwave Theory and Techniques, IEEE Transactions on ,* vol.24, no.4, pp. 195- 200, Apr 1976

[33] Gomes Neto, A., da Rocha, C.S., Bajon, D., Baudrand, H., "Analysis of the conductor-backed coplanar waveguide by an alternative formulation of the transverse resonance technique," *Microwave and Optoelectronics Conference, 1995. Proceedings., 1995 SBMO/IEEE MTT-S International*, vol.2, no., pp.851-855 vol.2, 24-27 Jul 1995

[34] Hatsuda, T., "Computation of Coplanar-Type Strip-Line Characteristics by Relaxation Method and its Application to Microwave Circuits," *Microwave Theory and Techniques, IEEE Transactions on ,* vol.23, no.10, pp. 795- 802, Oct 1975

[35] Selvan, P.T., Raghavan, S., Suganthi, S., "Multilayer Perceptron Neural model for Conductor- Backed Edge Coupled coplanar waveguides," *Electromagnetic Interference & Compatibility, 2008. INCEMIC 2008. 10th International Conference on ,* vol., no., pp.373-377, 26-27 Nov. 2008

[36] H. Kober, *Dictionary of Conformal Representations*. New York, NY: Dover Publications, 1957, pp. 52, 141

[37] Hilberg, W., "From Approximations to Exact Relations for Characteristic Impedances," *Microwave Theory and Techniques, IEEE Transactions on* , vol.17, no.5, pp. 259- 265, May 1969

[38] R. E. Collin, *Foundations for Microwave Engineering*, 2nd ed. New York: Mc Graw-Hill, 1992

[39] Weber, Ernst, "Mapping of Fields," *American Institute of Electrical Engineers, Transactions of the* , vol.53, no.12, pp.1563-1570, Dec. 1934

[40] F. B. Hilderbrand, *Advanced Calculus for Applications*, London: Prentic-Hall, 1948